ENGINE PISTON TEMPERATURE MEASUREMENTS FOR THERMAL LOADING USING A FIBER BRAGG GRATING (FBG) EMBEDDED INTO THE PISTON SURFACE

by

Dennis M. Ward

A thesis submitted in partial fulfillment of the requirements

for the degree of

MASTER OF SCIENCE

(Mechanical Engineering)

At the

University of Wisconsin - Madison

2004

I certify that I have read this thesis and that in my opinion it is fully adequate, in scope and quality, as a thesis for the degree of Master of Science.

Xiaochun Li
(Principal Advisor)

ABSTRACT

ENGINE PISTON TEMPERATURE MEASUREMENTS FOR THERMAL LOADING USING A FIBER BRAGG GRATING (FBG) EMBEDDED INTO THE PISTON SURFACE

Dennis M. Ward

Under the supervision of Professor Xiochun Li

at the University of Wisconsin - Madison

Optical fiber sensors have undergone refinements recently that make them attractive alternatives for traditional measurement devices. Optical fiber sensors are compact in size, easy to install and relatively inexpensive. These features have made them an ideal measurement tool for taking piston temperature measurements.

This project investigated embedding an optical fiber sensor into a metal piston, calibration of the sensor and the feasibility of measuring piston temperature with three different light sources. The fiber Bragg grating (FBG) sensor was used in this research was commercially purchased. A detailed procedure was developed that used a low temperature electroplating process to fully embed the FBG sensor into a small utility engine piston. The embedded sensor was calibrated by measuring the wavelength shift of the FBG and comparing it the temperature as measured by a thermocouple.

Of the light sources investigated, two were wavelength scanning lasers while the third was a broadband source. Attempts to measure piston temperature with the broadband source were unsuccessful due to the large light loss through the system. The wavelength scanning lasers used were both successful in measuring piston temperature in a non-contact manner. Due to cycle-to-cycle variations in the light transmission efficiency the slow scanning laser could only measured the piston temperature after the engine had been stopped. After running the engine at 1700 RPM with a load of 710 kPa IMEP the maximum piston temperature measured was 149 ^{0}C. The fast scanning laser technique measured the piston temperature with the running engine at the same conditions to be 136 ^{0}C. Comparing the results from both temperature measurements yielded only a discrepancy of 13 ^{0}C, which is believed to be good correlation.

ACKNOWLEDGEMENTS

To those that gave me a chance to study at the University of Wisconsin – Madison, especially the Wisconsin Small Engine Consortium (WSEC) members and those that made my time in Madison enjoyable, thank you.

TABLE OF CONTENTS

LIST OF FIGURES

LIST OF TABLES

NOMENCLATURE

BDC	Bottom Dead center
BTDC	Before top dead center
CO	Carbon monoxide
COV	Coefficient of variation
ECDL	External cavity diode laser
FBG	Fiber Bragg grating
FSR	Free spectral range
IMEP	Indicated mean effective pressure
NA	Numerical Aperture
OSA	Optical spectrum analyzer
PVD	Physical vapor deposition
RPM	Revolutions per minute
SLED	Superluminescent light-emitting diode
TIR	Total internal reflection
uHC	Unburned hydrocarbons

1 INTRODUCTION

1.1 Motivation

All materials, including the metals most frequently used in internal combustion engines decrease in tensile strength per density as the material temperature increases as can be seen in Figure 1-1. With more widespread use of small utility engines in daily life and increasingly tighter emissions regulations, engine designs have been forced to maximize power while minimized material and, therefore, cost. This has resulted in more efficient designs, but also less of a built-in safety factor in components, forcing each components function to be understood in detail. One of the most changeling components to analyze is the piston due to its reciprocating motion, however the piston remains one of the most important components of small engines with respect to durability. The piston contributes on the order of 50 to 60% of the mechanical losses of the engine [2]. Energy from combustion heats the crown of the piston and this heat needs to be dissipated by way of the ring pack and skirt.

Aluminum is a much better conductor of heat than cast iron. If silver is considered to be 100%, aluminum and cast iron have conductivities or 38 and 11.9% relative to that of silver. Aluminum, due to its high diffusivity greatly reduces the maximum operating temperature of the piston crown. Piston temperate is influenced by many factors including engine speed, load and combustion chamber design. The impact of engine speed is represented in Figure 1-2. One of the major disadvantages of aluminum is that it has a high coefficient of linear expansion. This means that the use of aluminum requires additional clearance be designed into the system so that at operating temperature excess friction is not generated. This additional clearance usually leads to piston slap when the engine is first started cold. Thus, to produce low noise with minimal impact on engine performance and to

ensure long engine life, being able to accurately measure piston temperature in a small engine is important.

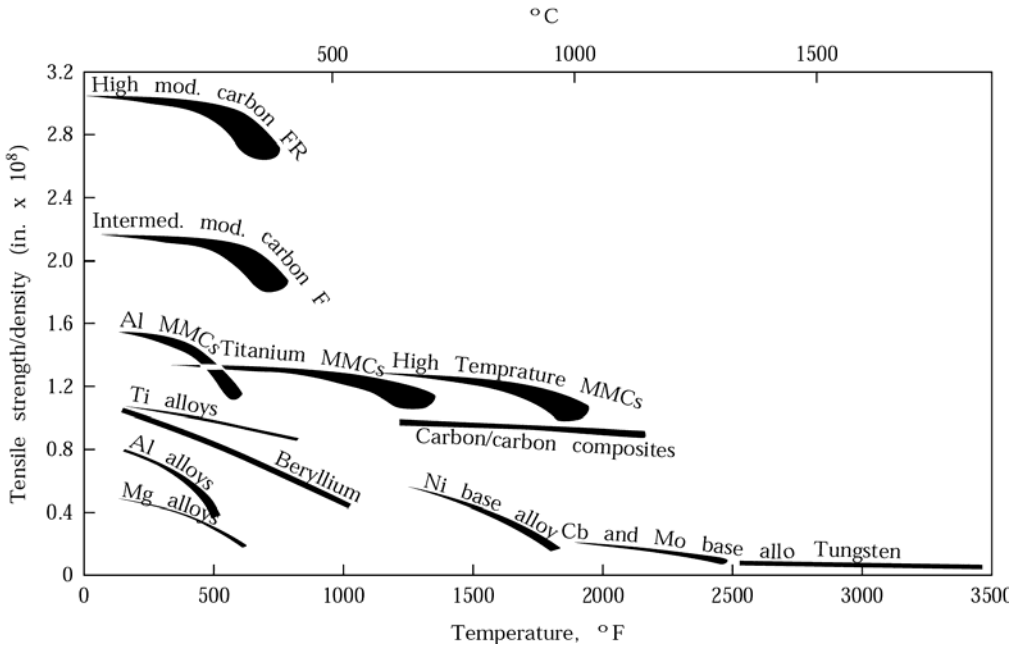

Figure 1-1 Specific strength of material versus temperature [1]

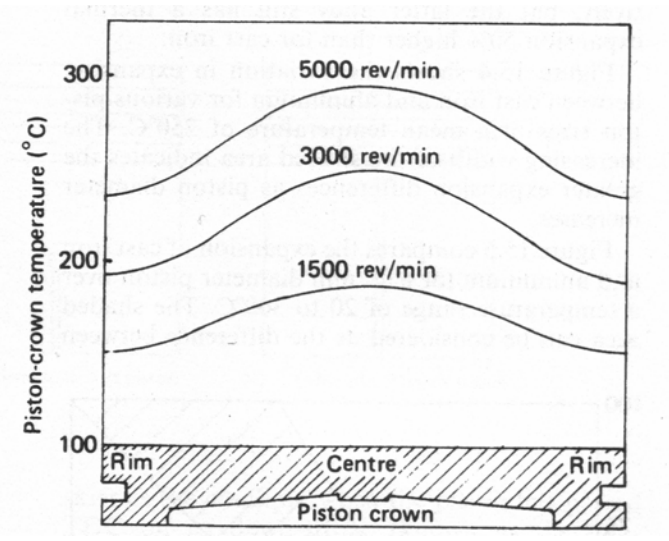

Figure 1-2 Piston crown temperature at various engine speeds [2]

1.2 Research Objectives

The objective of this research was to investigate piston temperature using an embedded fiber Bragg grating (FBG) and fiber optics with the least modification to the engine and intrusion on its operation. Three different light sources were used in an investigation to use a FBG as a temperature measurement device. One method involved a broadband light source while the other two methods involved a wavelength scanning light source.

Detailed descriptions of the embedding and engine modification processes are covered. In order to obtain an absolute temperature a static calibration test was performed to determine how the Bragg wavelength shift relates to temperature as measured by thermocouples. It was found that the wavelength shift relationship to temperature was linear and correlated well to literature values for measuring temperature with the FBG technique. This calibration curve was then used to determine the temperature measured in an engine running at 1700 RPM and partial load using a fast scanning laser and compared to temperature measurements taken at the same load condition but with the engine stopped.

1.3 Outline of the Work

In the following chapter a review of the literature on engine thermal experiments and measurements are discussed. Also, the method of embedded sensors for ‘smart structures’ is discussed with background on the technique used in this research. Chapters 3 and 4 give a detailed account of the hardware used in the experiment and the modifications to the engine to obtain optical access. Details of the sensor embedding process and characterization of the sensor are also discussed in Chapter 4. The methods used to measure piston temperature and

their results are in Chapter 0. The discussion of the results is given in Chapter 6 along with the conclusions obtained from this work and recommendations for future work.

2 BACKGROUND & LITERATURE REVIEW

2.1 Engine Thermal Theory

Developing an understanding of engine thermal loading has been a complicated and arduous process that has involved many researchers. Significant amounts of time have been devoted to investigations of a variety of engine types and components, however in spite of this effort solving engine heat transfer problems is still a major design task. Peak combustion temperatures are in the order of 2500 K, but to eliminate fatigue cracking metal temperatures must be kept nearly an order of magnitude lower. This problem is complicated further with portions of an engine receiving heat fluxes as high as 10 MW/m^2 during the combustion period with virtually no heat transfer a short time later [3]. This necessitates a robust cooling method and emphases the need to know maximum component temperatures for sustained engine durability.

Heat transfer affects engine efficiency, emissions, performance and durability considerably. Power and efficiency are affected by the magnitude of engine heat transfer with higher heat transfer to the combustion walls lowering the energy available for work recovery. Excess heat transfer to the engine can also have a critical effect on engine out emissions if the temperature drops too low to support afterburning of carbon monoxide (CO) and unburned hydrocarbons (uHC). The cylinder temperature also governs piston and ring oil film temperatures, and hence its viscosity and ability to lubricate, which can, in turn increase the friction generated leading to rapid component wear and premature failure.

2.2 Experimental Piston Temperature Methods

Most likely the first attempt to measure the temperature of the piston in an internal combustion engine was done in 1926 by Gibson [4]. The engine was run at the desired condition of interest until the engine conditions were stable; the engine was then stopped. Removing a spark plug allowed a thermometer to be inserted into a small cavity in the piston. A temperature versus time plot was then recorded and extrapolated back to the time when the engine was stopped to estimate the running piston temperature.

Other attempts have been made at using a thermocouple and a continuous electrical connection. The thermocouple wire was attached to the piston and then allowed to hang in a free loop to accommodate the reciprocating motion of the piston. This method worked fairly well, but was prone to failure as engine speed increased. To improve the robustness of this technique Baker [5] used a two-bar linkage mechanism to guide the wires outside of the crankcase with springs helping to absorb the wire flexing. With this improvement the measurement technique could now withstand 1400 RPM indefinitely.

To circumvent breaking thermocouple wire leads a number of investigators turned to an intermittent contact method where the electrical circuit is completed at one end of its stroke [6,7,8]. This technique has the advantage of allowing varying test conditions to be run. The intermittent contact method can be split into two groups: impact contact and sliding contact. As speed increases the impact contact method fails due to bouncing of the contact points due to the springs used to ensure electrical contact with piston movement. The sliding method uses contacts that rub each other and appear better suited to higher engine speeds as reported by Underwood et al. [8]. The main disadvantage of the contact method is that electrical contact is only made for a short period of time and occurs when the piston is at the

part of the engine cycle when the least pressure and temperature are in the combustion chamber. Due to the pistons reciprocating motion is the contacts were placed higher in the stroke, they would interfere with the engines operation. This method is also limited to the number of contacts that can be used due to the confinement of the crankcase.

Work on smaller engines and two-cycle engines with a minimum amount of room in the crankcase led to the use of the thermocouple wires being routed via a tube out through the combustion chamber. This method required a sealing mechanism to contain the combustion gasses and a system to cool the wires inside the tube to prevent weakening of the wire insulation. However, this method also suffered wire fatigue at higher engine speeds and was limited to 300 RPM [9].

The latest method utilized to transfer thermocouple signals outside the engine uses telemetry [10]. On the underside of the piston a transmitter is mounted, which transmits thermocouple information as frequency modulated infrared pulses. A photo detector mounted in the crankcase, which is wired to an external receiving unit, picks up this signal. This signal was successfully transmitted up to 5000 RPM with an accuracy of ±2.8°C. An improvement on this technique replaced the infrared transmitter with a microwave transmitter [11]. This removed the line of sight constraint for this method. This technique experiences several problems in that the transmitter batteries need replacement and the transmitter box can add a substantial amount of mass to the piston making its application use limited.

A recent method developed to measure piton temperature uses thermistors and electromagnetic induction. Transmitter and receiver coils are installed in the bottom of the cylinder and a resonator coil is installed onto the bottom of the piston. When alternating

current is applied to the transmitter coil a magnetic field and current is generated in the receiver coil. When temperature increases the embedded thermistor resistance decreases and the current flowing through the receiver coil decreases. Piston temperature can then be determined from a predefined map of current change and piston temperature. As reported by Kato [12] this method has many advantages including high accuracy of ±2.5°C, multiple measurement points per piston (six were demonstrated) and durability at speeds up to 6000 RPM. This method does suffer from a larger dispersion due to the D/A conversion maps making it inferior to thermocouples to track dynamic changes quickly.

As an alternative to thermocouple testing a metallurgical plug that could measure temperature based on thermal tempering was developed in the 1970's. This steel set screw can be used to determine the maximum temperature sustained in challenging locations such as a piston. Under ideal conditions this method is accurate to 3% [13]. However, long running times are needed to undergo the thermal tempering and multiple test conditions require disassembly and timely analysis. In addition, short temperature spikes cannot be measured limiting this methods usefulness.

2.3 Metal Embedded Smart Sensors

Fiber optic sensors embedded in structures provide new possibilities for testing. Using this technology, it may be possible to build a fully encapsulated sensing arrays that will be able to provide condition monitoring of parts while in operation. This is possible due to fiber optic sensor's ability to collect spatial and temporal data in large quantities.

Applications for embedding optical sensors span many areas including monitoring structural components in building and bridges [14], molds and tools in manufacturing [15],

pipes and containers in power generation [16] and engine conditions in the automotive industry [17].

The dominant use of embedded optical fibers in the last twenty years has been in non-metallic composites [18]. They are a convenient method to monitor important factors and components while being easy to embed in the manufacturing process. Optical sensors also provide the added benefit of being lightweight, immune to electromagnetic interface and resistant to hostile environments. However only a few researchers have used them as sensors to monitor conditions without continuous fiber contact [19], and still fewer have tried to use optical fiber sensors in hostile environments.

2.4 Principal of Fiber Bragg Gratings

Fiber optic light guides are usually glass, quartz or plastic and consist of a core and cladding. In addition, most fiber optics have a polymer coating on the outside to increase the fiber toughness. A typical fiber is schematically represented in Figure 2-1. Light propagates in the optical fiber by total internal reflection (TIR) because of the difference of index of refraction between the cladding and the core. The outer cladding material typically has a lower index of refraction than the core and light is guided along the length of the optical fiber when it satisfies the condition:

$$\sin \beta_{\min} > \frac{n_2}{n_1} \tag{2.1}$$

where β_{min} is the angle shown in Figure 2-2 and n_1 and n_2 are the indices of refraction of the core and cladding, respectively. In order for light to couple into the fiber it must be incident within an acceptance cone. The acceptance angle is related to the refractive indices of the core, cladding, and medium surrounding the fiber. This relationship is called the numerical

aperture (NA) of the fiber. Figure 2-2 illustrates the relationship between the acceptance angle and the refractive indices. By using Snell's law and basic trigonometric relationships, the NA of the fiber is given by:

$$NA = (n)\sin\beta_{\min} = \sqrt{(n_1^2 - n_2^2)} \qquad (2.2)$$

where n is the NA of the material outside of the fiber. Light entering the fiber from outside the acceptance cone strikes the core-cladding interface at too steep of an angle and enters the cladding, where it quickly dissipates.

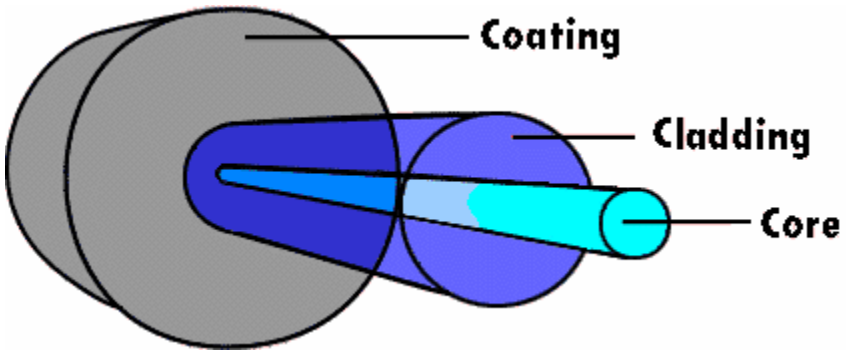

Figure 2-1 Fiber optic cable

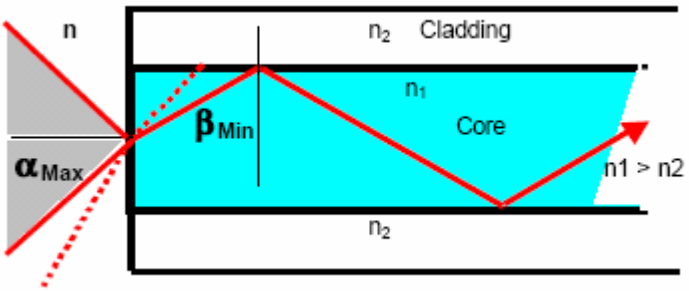

Figure 2-2 Light transmission in fiber optic cable

The photosensitivity of fibers was first observed in 1978 by Hill *et al* [20,21] and spawned a new technique for the measurement of temperature and strain. In its simplest form a FBG consists of a periodic modulation of the refractive index in the core of a single-mode optical fiber. In a uniform fiber Bragg grating, the phase fronts are perpendicular to the fiber's longitudinal axis with grating planes having constant period as shown in Figure 2-3. Light, guided along the core of an optical fiber, will be scattered by each grating plane. If the Bragg condition is not satisfied, the reflected light from each of the subsequent planes becomes progressively out of phase and will eventually cancel out. Additionally, light that is not coincident with the Bragg wavelength resonance will experience very weak reflection at each of the grating planes because the index mismatch. For wavelengths where the Bragg condition is satisfied, the contributions of reflected light from each grating plane add constructively in the backward direction to form a back-reflected peak with a center wavelength defined by the grating parameters.

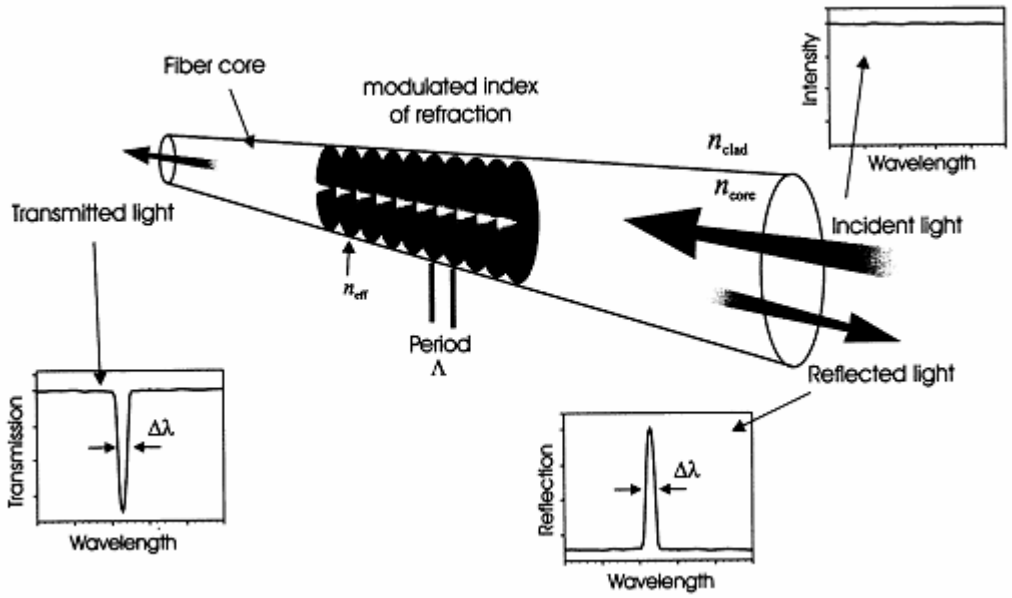

Figure 2-3 Fiber Bragg Grating schematic [22]

The Bragg grating resonance, which is the center wavelength of back-reflected light from a Bragg grating, depends on the effective index of refraction of the core and the periodicity of the grating. The simple relationship is shown as

$$\lambda_B = 2n_{eff}\Lambda \tag{2.3}$$

Where λ_B is the Bragg wavelength, n_{eff} is the effective index change and Λ is the distance between index of refraction changes. The effective index of refraction as well as the periodic spacing between the grating planes is affected by changes in strain and temperature. If (2.3) is differentiated the shift in the bragg grating center wavelength due to strain (Δl) and temperature (ΔT) changes is given by:

$$\Delta\lambda_B = 2\left(\Lambda\frac{\partial n_{eff}}{\partial l} + n_{eff}\frac{\partial\Lambda}{\partial l}\right)\Delta l + 2\left(\Lambda\frac{\partial n_{eff}}{\partial T} + n_{eff}\frac{\partial\Lambda}{\partial T}\right)\Delta T \tag{2.4}$$

The strain effect on an optical fiber is represented by the first term in equation (2.4). This change is induced by two phenomena the physical change in grating spacing and the strain induced change in the refractive index. Experimental results show that for an applied 500 με the Bragg center wavelength will shift approximately 1 nm as shown in Figure 2-4.

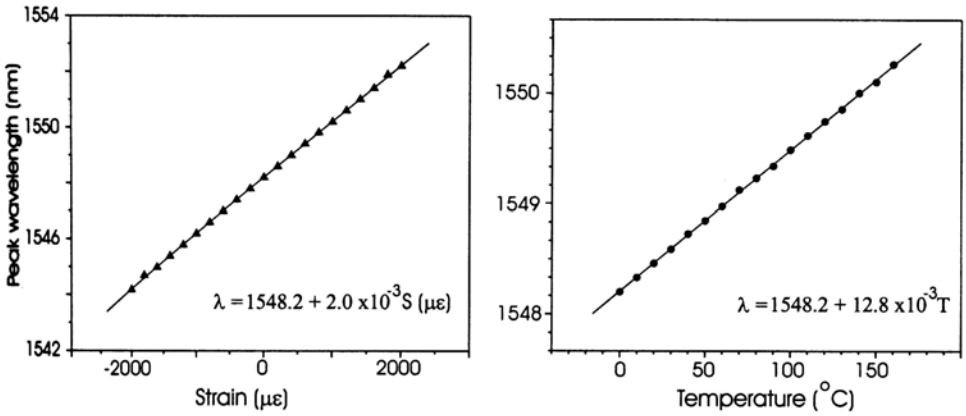

Figure 2-4 Temperature and strain effect on a Bragg grating [22]

The temperature effect on an optical fiber is represented by the second term in (2.4). The Bragg wavelength shifts due to changes in the grating spacing by thermal expansion and the changes in index of refraction. If this effect is studied alone the wavelength shift for a temperature change ΔT can be written as:

$$\Delta\lambda_B = \lambda_B(\alpha_\Lambda + \alpha_n)\Delta T \qquad (2.5)$$

Where α_Λ is the thermal expansion coefficient for the fiber and α_n represents the thermo-optic coefficient, which are respectfully equal to approximately 0.55 x 10^{-6} and 8.6 x 10^{-6} [22]. Observing the temperature effect on the Bragg wavelength in Figure 2-4, the sensitivity of a Bragg grating is approximately 1.28 nm per 100 ^{0}C. It should be noted that any change

in wavelength caused by an external excitation to the grating is the sum of both the temperature and strain effects, thus, if used in a sensing application where only one perturbation is of interest, the separation of temperature and strain becomes necessary.

3 PROJECT EQUIPMENT

3.1 Test Engine

The engine used in this investigation was a Briggs & Stratton, Intek model 110602. It is a 4.8 kW (6.5 hp) vertical crankshaft single-cylinder spark-ignited engine. The engine is air cooled, with the airflow provided by vanes cast into the flywheel. The complete Briggs & Stratton Intek engine specifications are given in Table 3.1.

Engine	Briggs & Stratton Intek model 110602 type 0015
Bore	68.275 mm
Stroke	45.720 mm
Displacement	167.38 cm^3
Connecting rod length	88.6 mm
Wrist pin offset	0.381 mm
Combustion chamber	Pancake Style
Geometric compression ratio	6.6:1
Valve configuration	Overhead, single intake, single exhaust
Rated speed	3060 rpm
Power rating	4.8 kW

Table 3.1 Test engine specifications.

The stock carburetor was a non-adjustable type, so the main jet was replaced with an adjustable jet so that allowed the mixture to be changed. This allowed the fuel-air mixture to

be changed. The engine was also equipped with a fixed magneto ignition system that would produce a spark 19^0 before top dead center (BTDC).

3.2 Engine Test Rig

An AC dynamometer was used to start, motor and control engine speed. The dynamometer was found to be capable of maintaining the set speed within 3 RPM motoring and 7 RPM while firing. The air delivery, fuel and exhaust system descriptions can be found in the thesis of Albert [23].

3.3 Engine Monitoring Apparatuses

A piezoelectric pressure transducer (Kistler model 6061) was installed into the engine's head to calculate the work transfer from the gas to the piston. With changing cylinder pressure a diaphragm compresses a quartz crystal that generates an electric charge proportional to the applied pressure [3]. A Kistler dual mode charge amplifier model 5010B was used to convert this charge output into a voltage. By using the calibration of the transducer the dynamic cylinder pressure can be obtained. The calibration curve of the pressure transducer is given in Appendix A. A Hi-Techniques HT-600 data acquisition system was used to record the cylinder pressure for 200 cycles. A C-program extracted the binary data and converted it to a text file. The program also calculated indicated mean effective pressure (IMEP), average peak pressure, the average crank angle of peak pressure and the coefficient of variation (COV) of IMEP. Water was circulated though the transducer to keep its temperature constant. The water was supplied to the transducer by an external pump drawn from a reservoir cooled by building water. Figure 3-1 shows the location of the pressure transducer in the cylinder head. The second center spark plug was added for other research and was not used for this project.

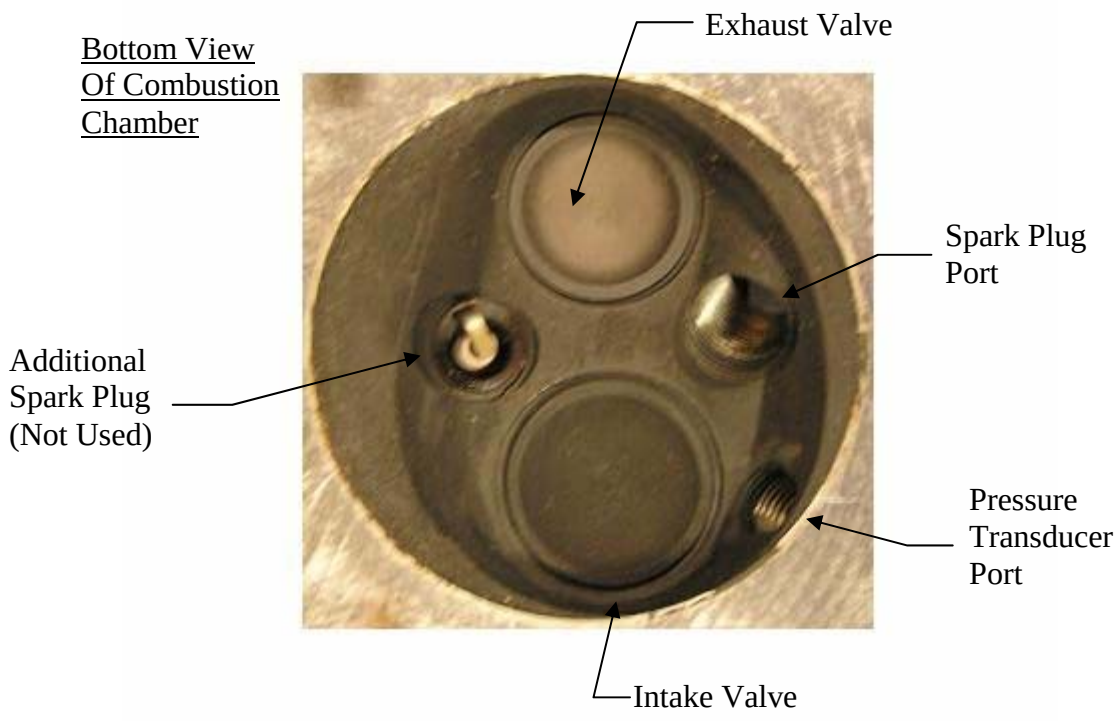

Figure 3-1 Pressure transducer location in the cylinder head

For setting and monitoring the engine operating conditions the air fuel ratio was measured. A Horiba Mexa-110 lambda sensor in the exhaust was used to determine the charge air fuel ratio and verify correct operation of the carburetor.

Engine temperatures were closely monitored to evaluate engine performance. These included the oil sump temperature, intake air and the exhaust gas. The first exhaust gas measurement was at the exit of the exhaust port and near the lambda sensor. This measurement made sure that the oxygen sensor was at proper temperature and not producing erroneous results due to water condensation. The second exhaust temperature located in a surge tank downstream in the exhaust was used together with the oil sump temperature to

give a point of reference as to when the engine had reached its steady state operating temperature during testing.

3.4 Optical System

Temperature can be measured with the FBG technique with four basic components: a light source, transmitting fiber optics, a FBG sensor and a photo detector. After being focused into a single-mode fiber the light is transmitted from the source to the engine. When the engine reaches bottom dead center (BDC) light is coupled into the sensor fiber when the pitching fiber is aligned in close proximity to the sensor fiber end. After the light passes through the sensor fiber, it is collected and focused onto a multimode fiber. Finally, the transmitted light intensity is measured, which can be converted into a temperature. Figure 3-2 shows the basic concept of the optical system used to measure temperature in an internal combustion engine with a FBG. The FBG and the embedding process is discussed in Chapter 4 while the remainder of the system will be covered in the following subsections.

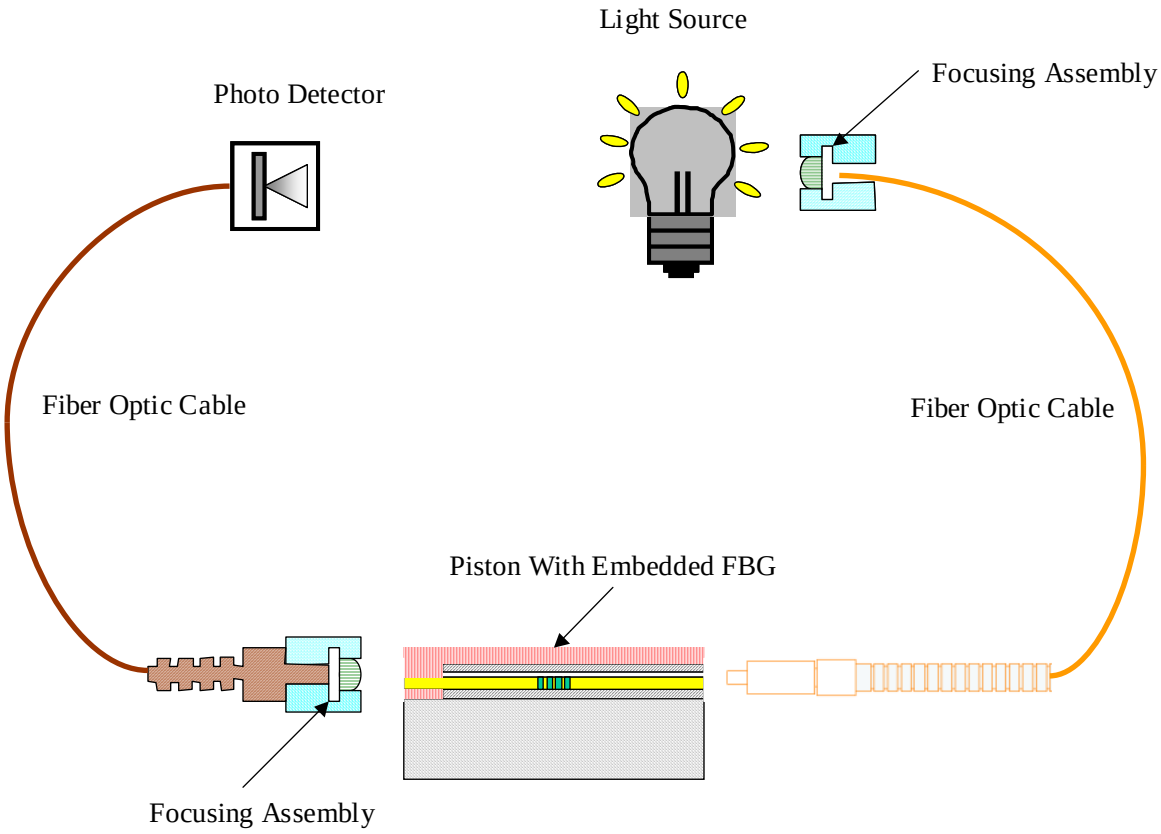

Figure 3-2 Temperature measurement technique

3.4.1 Fiber Optics

The optical fibers in contact with the engine were metal-jacketed silica fibers manufactured by Oxford Electronics Limited. The fibers consist of an inner core, an intermediate cladding and an external metal jacket. Light incident on one end of the fiber is transmitted through the core by total internal reflection from the cladding due to a higher index of refraction in the core material. The core of the input fiber has a diameter of 9 μm and is made of pure silica. The cladding has an outer diameter of 125 μm and is made of a doped fused silica. Finally, the copper jacket has a diameter of 190 μm. The copper jacket was chosen for its added ability to withstand higher temperatures and increased overall

strength compared to a polymer-coated fiber. To increase the overall robustness of the fiber assembly a stainless steel sheath covered the fiber. These were important considerations when working with the high temperatures and vibrations generated by the engine. To make coupling light into the fiber easier each end of the fiber had a FC connector that could be mated to the light source.

The collection fiber consisted of a 600 μm core, 636 μm cladding and a 750 μm diameter aluminum jacket with SMA-905 connectors in a stainless steel sheath. This fiber was chosen for its large core size to facilitate collecting as much light as possible.

To position the end of the single mode fiber carrying the signal light to the sensor fiber a translation stage was used. This stage allowed for adjustment in all three dimensions via 80 thread per inch screws. The whole assembly could be fixed in place with locking screws. For rigidity the translation stage was mounted to the engine block with 0.25 inch aluminum supports. When the end of the launching fiber was adjust to have 0.73 mm of space between it and the end of the sensor fiber a 200 μm spot was projected onto the end of the sensor fiber due to the natural dispersion of light exiting the fiber. This large spot size would help to allow for misalignment and movement of the sensor end on a cycle to cycle basis.

To collect the light emerging from the embedded FBG sensor fiber a collimation lens assembly was used. This assembly (Thor Labs F230SMA-C) combined an antireflective coated lens into an aluminum housing. The lens was positioned such that it was one focal length away from the end of the fiber.

3.4.2 Light Source

Multiple light sources were used in this project and included a broadband and two laser sources with scanning capabilities. To differentiate between the two scanning lasers the commercial tunable diode laser with maximum scanning speed of 26.74 nm/sec will be referred to as the slow scanning laser. The other laser, which was constructed at the University of Wisconsin – Madison, has a scan rate of 2.4×10^6 nm/sec which will now be referred to as the fast scanning laser.

3.4.2.1 Superluminescent Light Emitting Diode

A Superluminescent Light-Emitting Diode (SLED) was sourced for a broadband light source. The SLED used was an Opto Speed (model 1400D20A) which was fiber coupled into single mode 9μm fiber with a FC connector. It was mounted on an ILX Lightwave laser diode mount with corresponding precision current source and temperature controller (models LDM-4980, LDX-3525 and LDT-5525, respectfully). At full current input the total power output was 2.65 mW covering 100 nm, with Figure 3-3 showing the region surrounding that used in this project.

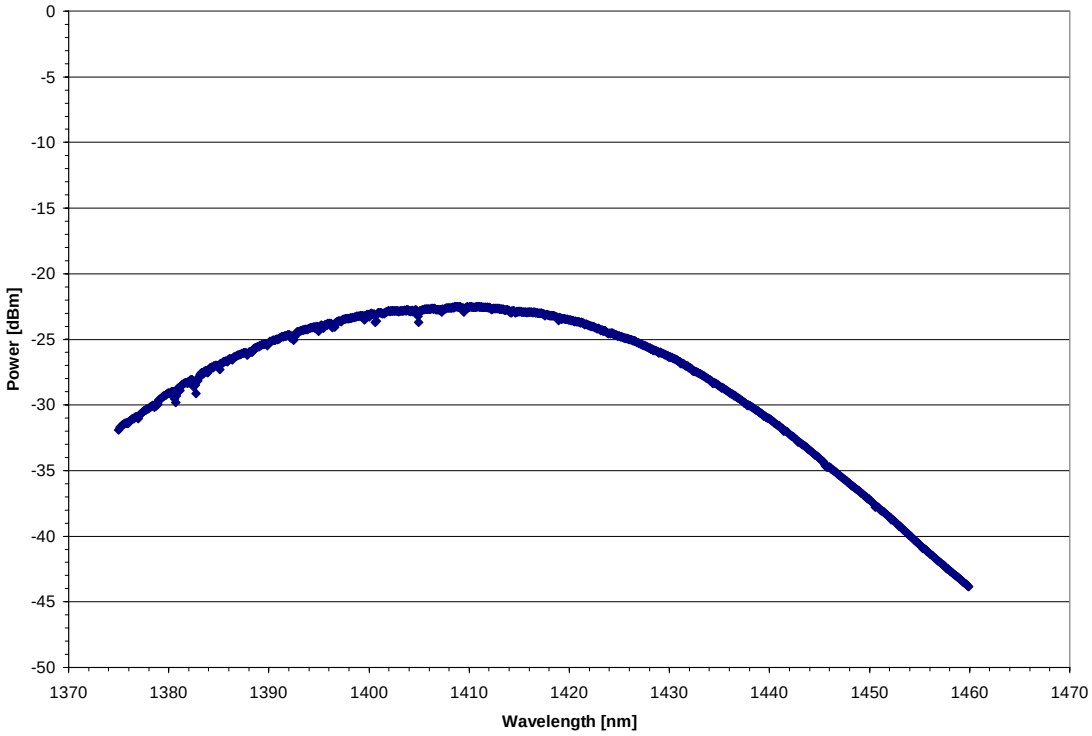

Figure 3-3 SLED maximum power output

3.4.2.2 Slow Scanning Laser

A commercially available New Focus 6327 tunable diode laser was used as the first agile wavelength source. The tunable laser was chosen because of its ability to scan a wide wavelength range in a relatively short amount of time. The wavelength range had infinite adjustment between 1380.4 and 1476.1 nm with scan times ranging from 0.01 to 26.74 nm/sec. The laser has a linewidth of 11.7 GHz and operates in single mode throughout the tuning range if the light power is adjusted to be less than 12 mW. This was verified by taking measurements at increasing levels of laser power output with an optical spectrum analyzer observing the traces, until multimode operation was observed at 12 mW. A sample trace of the laser operating at 1% of its peak power is shown in Figure 3-4.

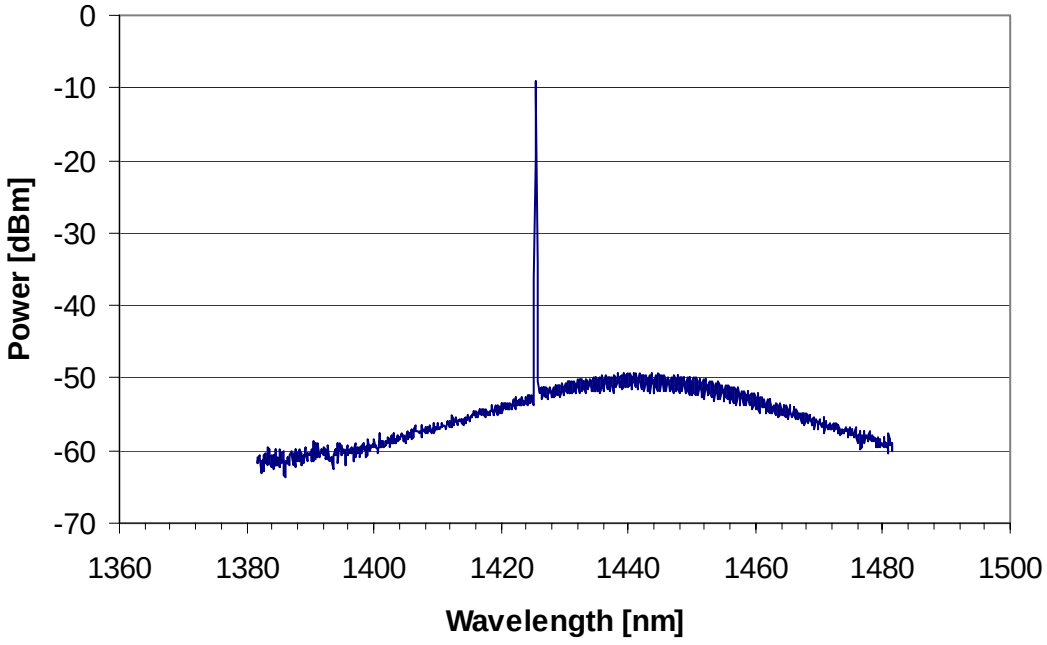

Figure 3-4 New Focus laser at maximum output

Scanning laser operation was also evaluated by recording a laser scan with time on a photo detector. The laser was set to scan from 1425.5 to 1428.5 nm with a speed of 1 nm/second. Single mode fiber optic patch cords delivered the light a PDA400 photo detector, of which specifications can be found in section 3.4.3. The photo detector output was recorded at 1 MHz with a Hi-Techniques HT-600. The resultant trace can be seen in Figure 3-5. This trace shows a periodic signal with large peaks arriving every 0.05 seconds, corresponding to a $\Delta\lambda$ of 0.05 nm. This periodic signal is caused by an etalon that has formed in the optical system. When light is passed between two flat, parallel, partially reflective surfaces an etalon is formed, as depicted in Figure 3-6. When monochromatic light

is passed through an etalon, multiple interference occurs producing fringes in intensity. The spacing of these fringes is related to the free spectral range (FSR) defined as:

$$FSR = \frac{c}{2 \cdot n \cdot d} \tag{3.1}$$

where c is the speed of light, d the spacing between reflecting surfaces, and n is the index of refraction of the material between the reflecting coatings. Knowing the FSR a distance and therefore likely source of the etalon can be calculated. The etalon formed in Figure 3-5 is from the spacing between the window and photo array in the photo detector. Proof of this is evident by the lack of the etalon in Figure 3-4. Another higher frequency etalon was also measured as shown in Figure 3-7. This etalon was calculated to be from the laser cavity it self.

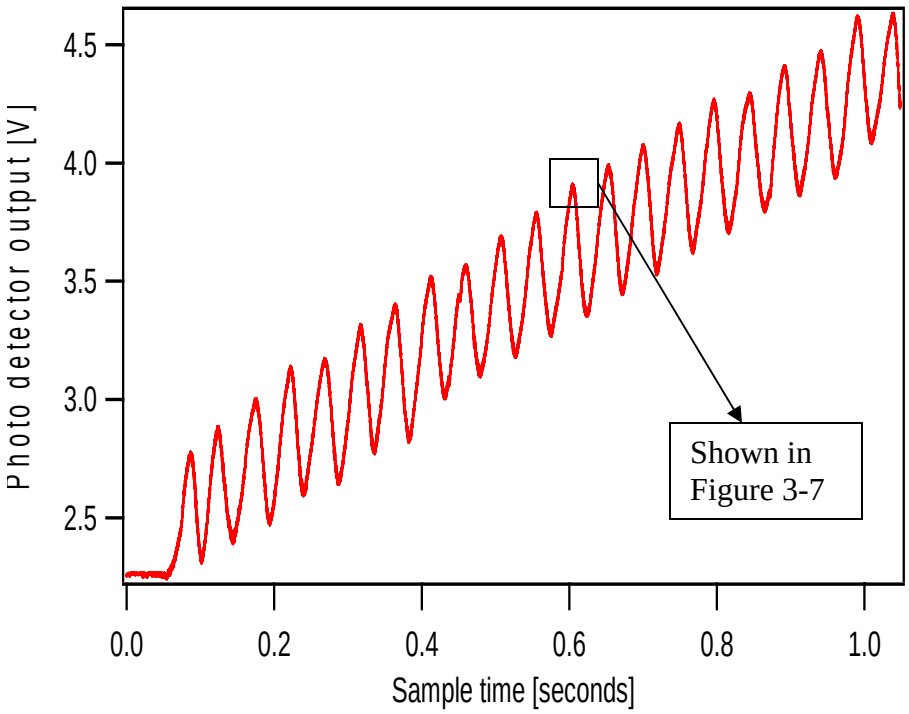

Figure 3-5 Slow scanning laser trace

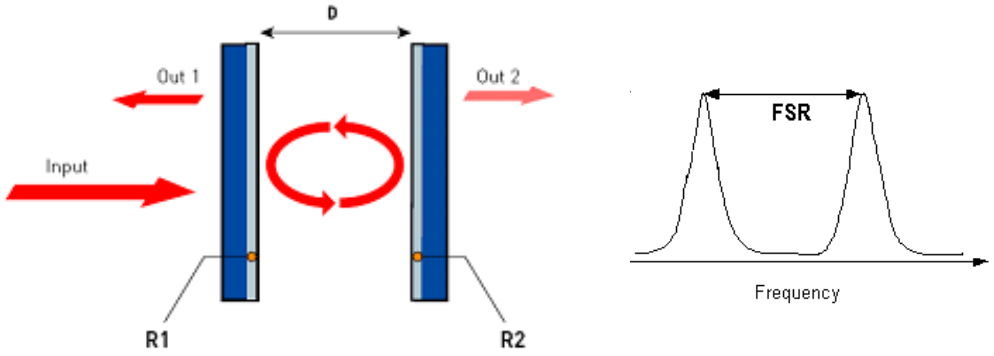

Figure 3-6 Etalon formation mechanism and result

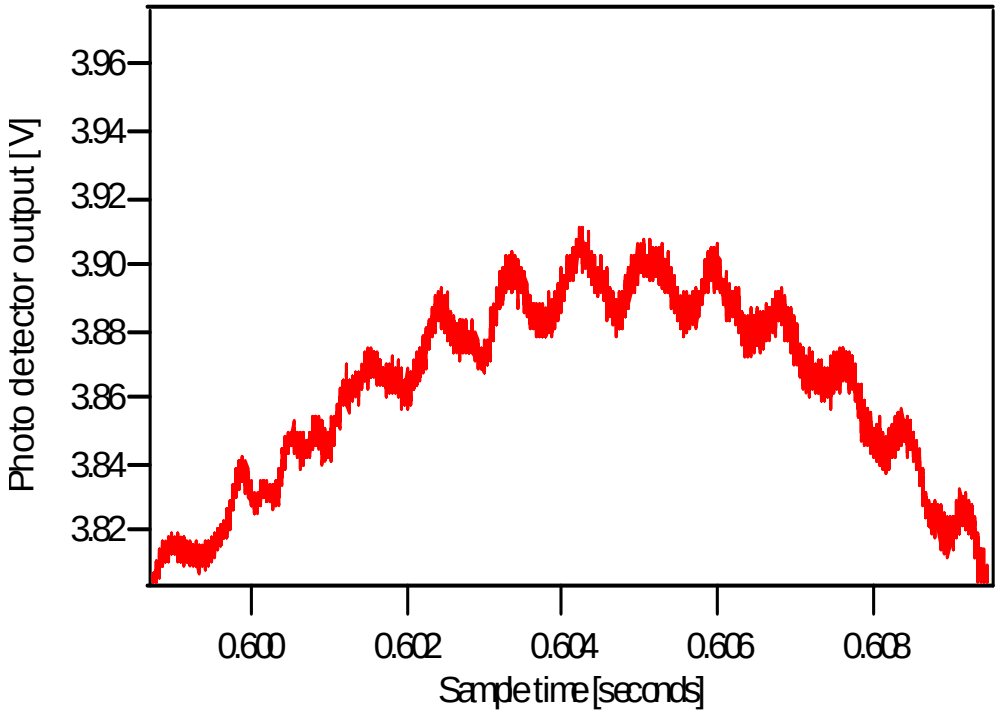

Figure 3-7 Slow scanning laser trace zoomed

The laser outputs a reference signal proportional to the wavelength produced that is used to determine an absolute temperature change. The voltage output is linear with respect to the wavelength of laser light and can be accessed through a BNC connector on the back of the control box. Figure 3-8 shows how the voltage corresponds to the wavelength as measured by an OSA. The voltage-to- wavelength relationship can be described as

$$\lambda = 16.499 * V + 1380.417 \tag{3.2}$$

where λ is in nm and V is in volts.

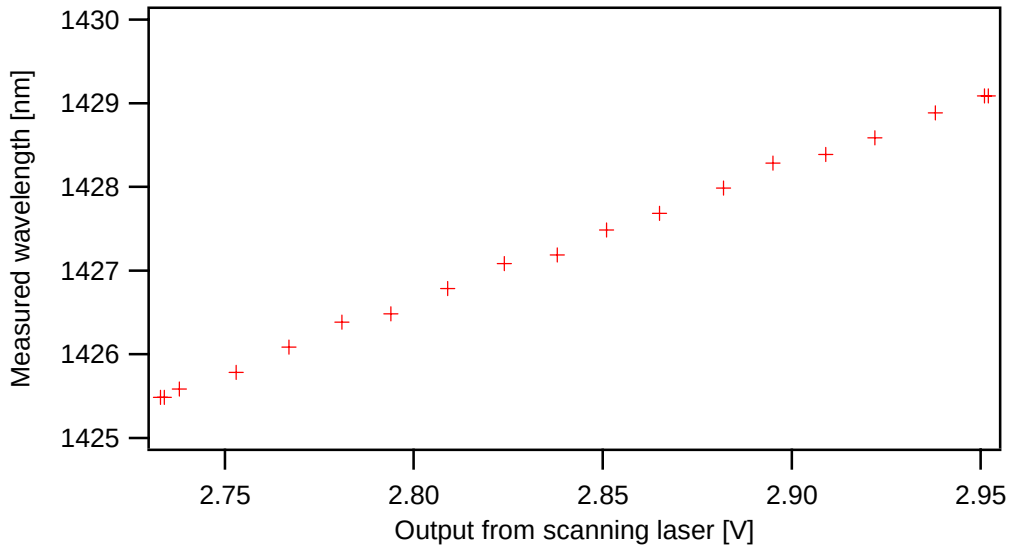

Figure 3-8 Wavelengths versus voltage output from tunable laser

3.4.2.3 Fast Scanning Laser

The fast scanning laser used in this project is similar to the one developed and used in Kranendonk [24]. The external cavity diode laser (ECDL) used in this research was modified to scan from 1420.20 to 1432.68 nm in 32 μs with 1.6 mW of total power coupled into a single mode fiber. The cavity consists of the diode, box beam splitter, grating, spherical mirror and a plane mirror. The plane mirror is mounted on a resonant scanner

vibrating at 15.6 kHz. The vibrating mirror forces the diode laser to sweep from 1420.20 to 1432.68 nm in 32 µs, and then to return from 1420.20 to 1432.68 nm in the next 32 µs. This scanning range can be seen in Figure 3-9 as measured by an OSA over a one second period. To avoid water absorption within the cavity the laser system is contained in a sealed box and purged with dry air.

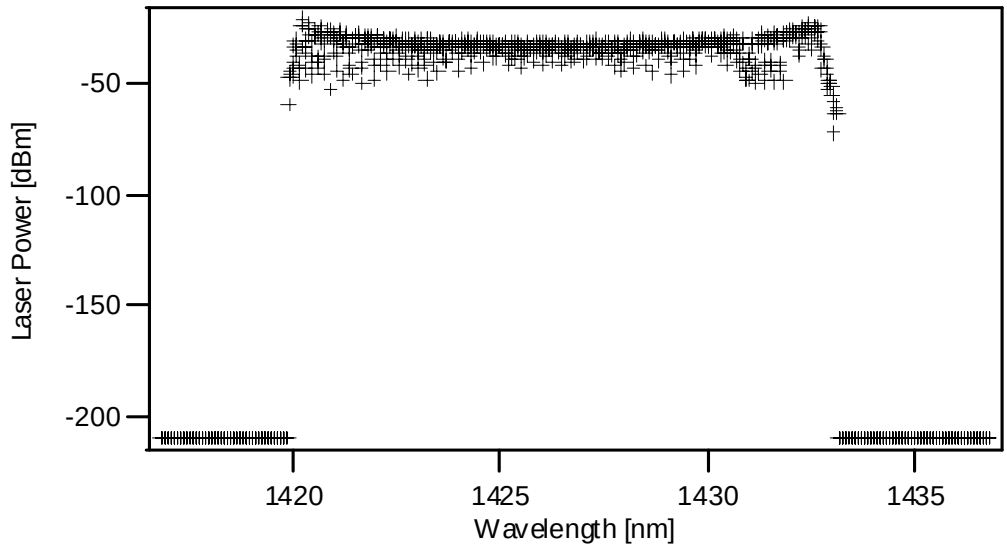

Figure 3-9 Fast scanning laser measured wavelength range

3.4.3 Detector

The main detector used in this project was a Thorlabs PDA400. The PDA400 is an amplified, switchable-gain, InGaAs detector designed for detection of light signals up to 10 MHz. It has a peak response of 0.95 A/W at 1550 nm. For the spectral range used in this project it has an average response of 0.86 A/W. This detector also has a large active area of 1 mm^2, which allows for the use of a large multimode fiber for the collection of light from the FBG fiber.

An optical spectrum analyzer (OSA) was also used for a spectral intensity measurement. The Agilent model 86143B OSA has many features that make it very versatile for the measurements taken in this project. It is capable of low light level detection with a sensitivity of –90 dBm. The OSA has an absolute accuracy ± 0.5 nm, but after internal calibration it is capable of a ± 0.06 nm resolution measurement. However, this resolution is based on a single mode input fiber. Since the OSA uses a diffraction grating to separate light into discrete wavelengths, the accuracy scales linearly with input fiber size. An FC port provides an easy method to connected signal patch cords. This particular OSA is limited to a sweep rate of 40 nm in 56.3 ms as stated by the manufacture.

4 EXPERIMENTAL SETUP

4.1 Outline of FBG Temperature Measurement Setup

In order to make a piston temperature measurement using the FBG technique specific hardware modification are required. Optical access ports are required in the cylinder and the FBG needs to be embedded into the piston surface. A schematic of the optical system is shown in Figure 4-1. The following section, 4.2, outlines the machining process of the cylinder block necessary and sections 4.3 and 4.4 cover the sensor embedding processes of machining and nickel electroplating.

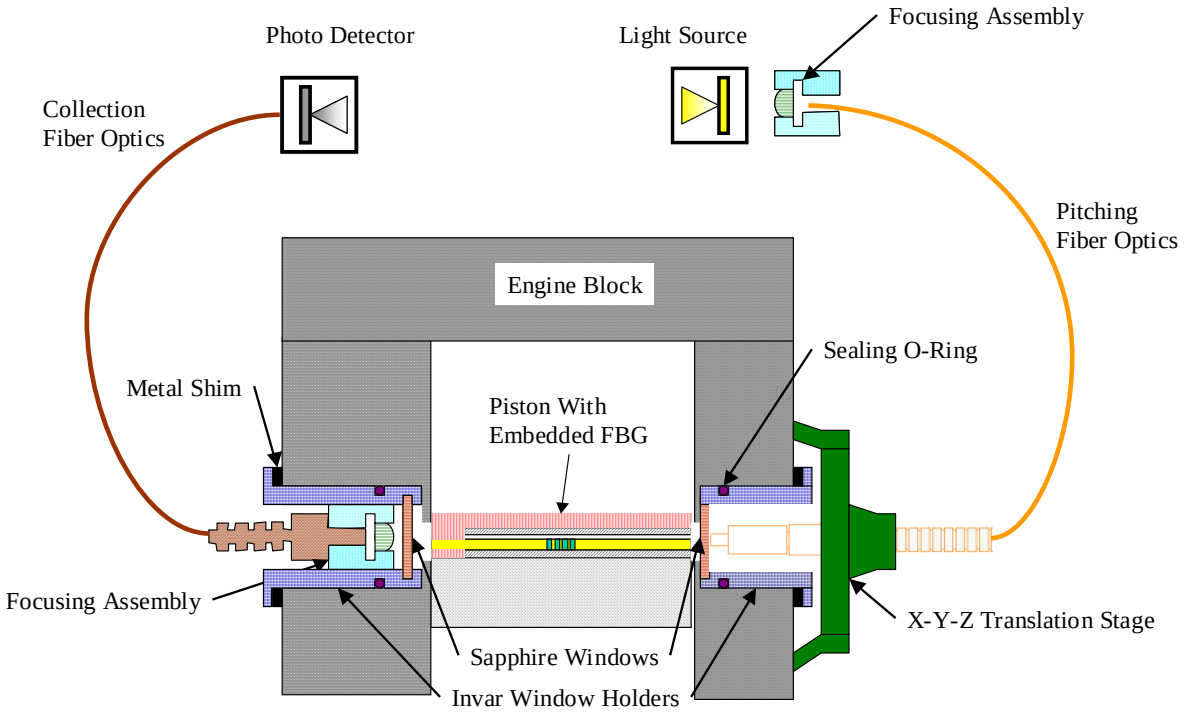

Figure 4-1 Optical engine section view with piston at BDC

The goal of this research was to measure a steady state maximum piston temperature. It would be essential to not have the measured piston temperature affected by the heat flux imposed by combustion on a cycle to cycle basis. In order to check the validity of this condition the material's time response to a heat input was evaluated. Using the properties of the embedding material, nickel, at an assumed maximum piston temperature of 400 K in the thermal diffusivity (α) of nickel could be estimated as in Equation 4.1.

$$\alpha_{400} = \frac{k}{\rho \cdot c_p} = \frac{80.2\left[\frac{W}{m \cdot K}\right]}{\left(8900\left[\frac{kg}{m^3}\right]\right) \cdot \left(485\left[\frac{J}{kg \cdot K}\right]\right)} = 18.6x10^{-6}\left[\frac{m^2}{s}\right] \qquad (4.1)$$

where c_p is the specific heat, ρ is the material density and k is the thermal diffusivity. Using the thermal diffusivity the time response, τ, can be calculated as in equation 4.2 with L being the distance below the surface that the FBG resides.

$$\tau \cong \frac{L^2}{\alpha} = \frac{\left(0.89x10^{-3}[m]\right)^2}{18.6x10^{-6}\left[\frac{m^2}{s}\right]} = 0.042\ [s] \qquad (4.2)$$

The maximum engine speed of the test engine used is 3060 RPM, which equates to one crank revolution in every 0.0196 seconds. Since the characteristic response time is more than 2 engine revolutions, it can be assumed that the measured piston temperature will be steady, unaffected by the periodic nature of the heat flux.

Fiber Bragg Gratings are sensitive to both temperature and strain. Since this project only wants to measure temperature the strain affect needs to be decoupled. To accomplish

this the FBG sensor was enclosed in a stainless steel tube. The tube was a 30-gauge hypodermic needle with a 152 μm nominal inside diameter and a 311 μm nominal outside diameter with the complete specifications given in Table 4.1. To secure the fiber to the piston the thrust side fiber end was allowed to extend out of the tube 3 mm and, therefore, was electroplated to the piston, as illustrated in Figure 4-2. The rest of the sensor fiber was enclosed in the tube and able to float, negating any strain effect cause by the surrounding material.

Material	Stainless Steel T-304
I.D.	152 μm
Tolerance	139.7 μm min
	177.8 μm max
O.D.	311 μm
Tolerance	304.8 μm min
	317.5 mm max

Table 4.1 Stainless steel tubing specifications

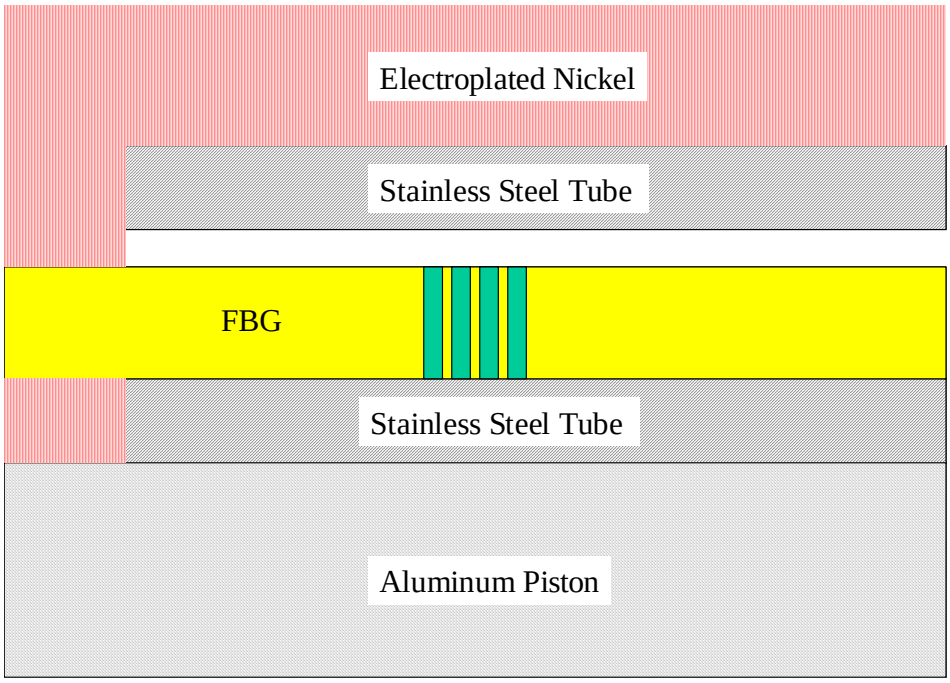

Figure 4-2 Separation of temperature and strain with a stainless steel tube

4.2 Engine Modifications

To gain optical access to the cylinder for this measurement two through holes were drilled into the block. The holes were perpendicular to the wrist pin axis; down from the deck surface the length of the stroke plus the depth of the embedded fiber in the piston (46.032 mm). These through holes were directly across the bore from one another since the FBG sensor would be embedded in a path straight across the piston. The collection side was located on the anti-thrust side of the engine with the optical access port passing through the push rod cavity adjacent to the crank case vent cavity. This side of the engine is shown in Figure 4-3 with the launching side similar.

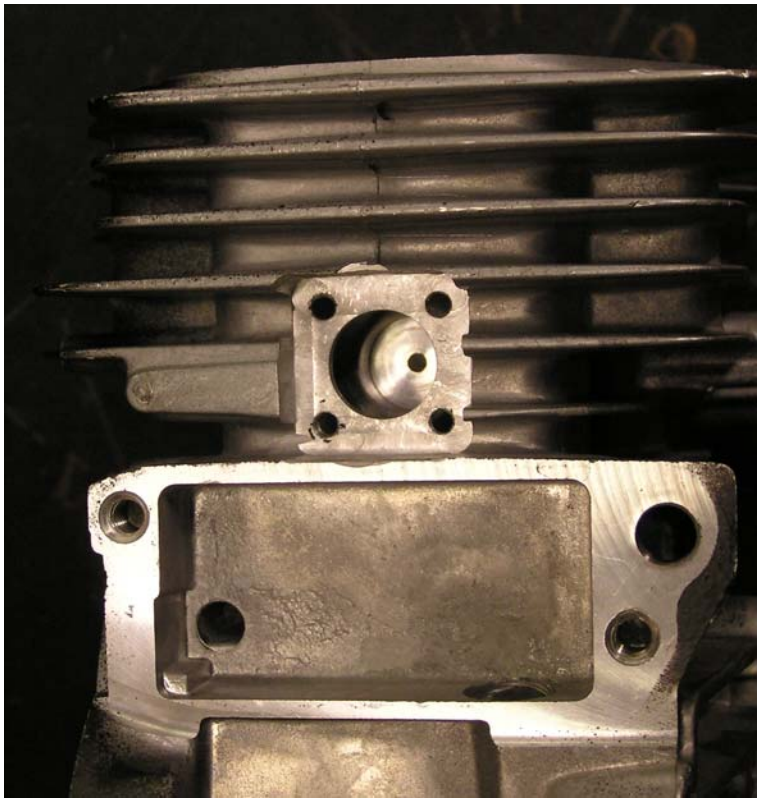

Figure 4-3 Light collection port in the machined engine block

To seal the combustion chamber or crankcase from the outside environment sapphire windows were used on both the input and collection sides. To minimize the intrusion into the engine the windows were kept as small as small as possible, while still allowing adjustment of the delivery fiber to account for any variation in manufacturing and to adjust for maximum signal transmission. The windows used were 9.525 mm in diameter and 0.508 mm thick.

To contain the windows and hold them in place are two window holders, which are shown in Figure 4-4. To place the windows as close as possible to the cylinder bore, two 12.700 mm counterbored holes were machined into the block concentric to the optical access ports. The depth of the counterbored holes left 0.051 mm of the block material between the

cylinder bore and the inside window surface. In addition to decrease the distance from the cylinder bore to the window face the sapphire windows were joined to the window holders with a ceramic adhesive (Cotronics Resbond 940). In order for this mounting method to be feasible with the large temperature changes that would occur, the window holders were constructed of Invar 36. The coefficient of thermal expansion of Invar 36 is one-tenth that of carbon steel up to 200 ^{0}C, thus making its thermal expansion within 50% that of sapphire. The cylinder block was also machined to accept the fasteners that secure the window holders. Each window holder had a viton o-ring to seal the combustion chamber from the outside environment with the collection side window holder having an additional o-ring to prevent oil leakage from the pushrod cavity. Final placement adjustments were possible through the use of metal shims between the engine block and the window holders. The launching side holder and window can be seen in Figure 4-5.

Figure 4-4 Invar window holders

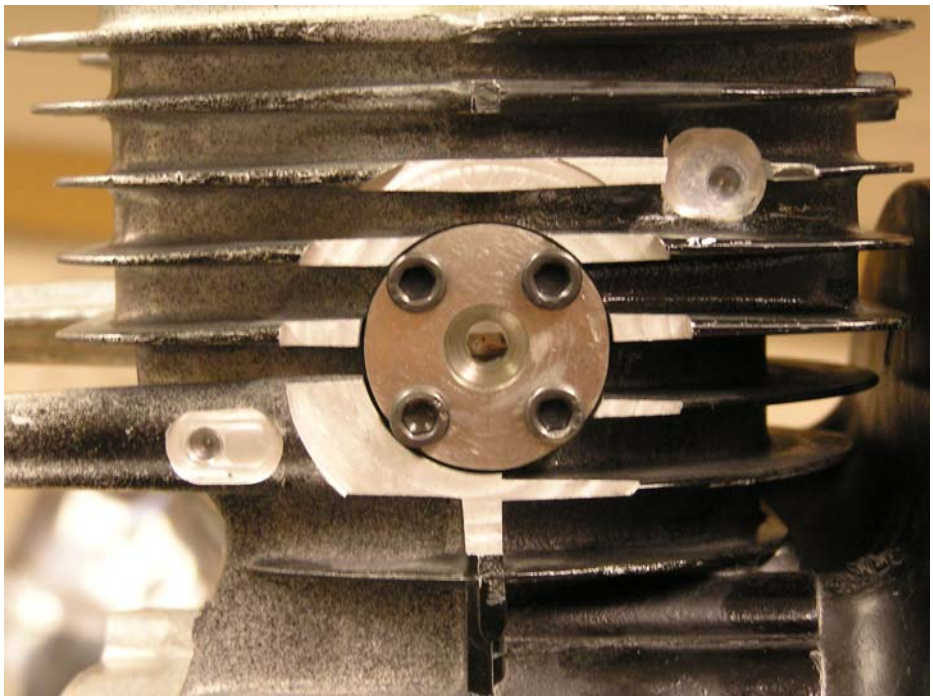

Figure 4-5 Launching side machined engine block with window and holder

4.3 Piston Modifications

To embed the FBG into the piston a channel was machined into the crown of the piston. The channel traverses the piston perpendicular to the wrist pin axis and on the piston centerline, thus aligning with the optical access ports in the cylinder block. In Figure 4-6 the dimensions of the groove can be seen along with a layout schematic. To more securely locate the FBG two locating bosses were left in the groove. Each boss was located 5.067 mm from the piston edge, was 7.62 mm thick, and had a 0.343 mm hole drilled through it to hold the FBG.

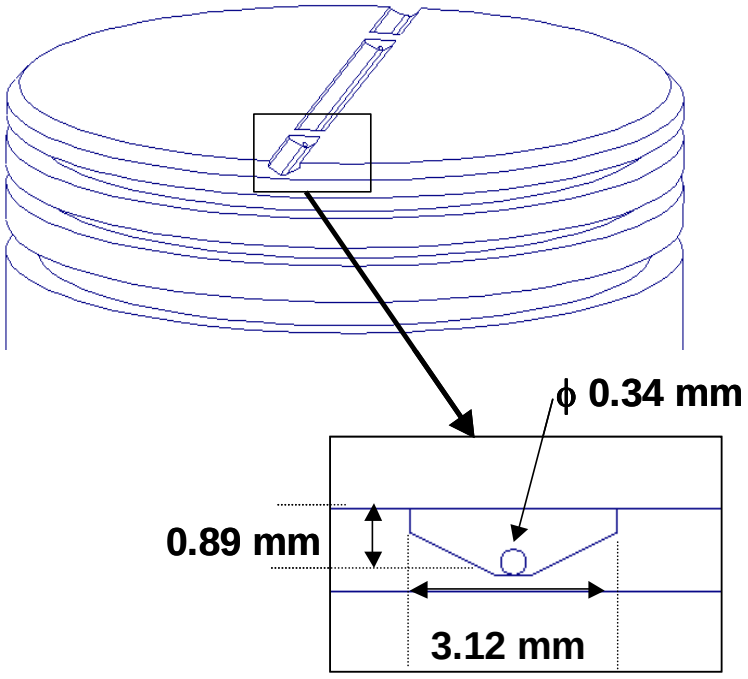

Figure 4-6 Piston channel dimensions

The engine used in this investigation has a standard ring design of two compression rings and one oil control ring. The compression rings were pinned to prevent them from turning as shown in Figure 4-7. This was done because piston rings rotate under normal operation as proven by various researchers [25,26]. The pin eliminated the possibility of the piston rings rotating and becoming caught in the optical access hole. The compression rings were assembled so that their gaps would be opposite at an angle of 180°. Due to the expander spring in the oil control ring a stopper pin was not used, but the free ends were given a 0.508 mm chamfer.

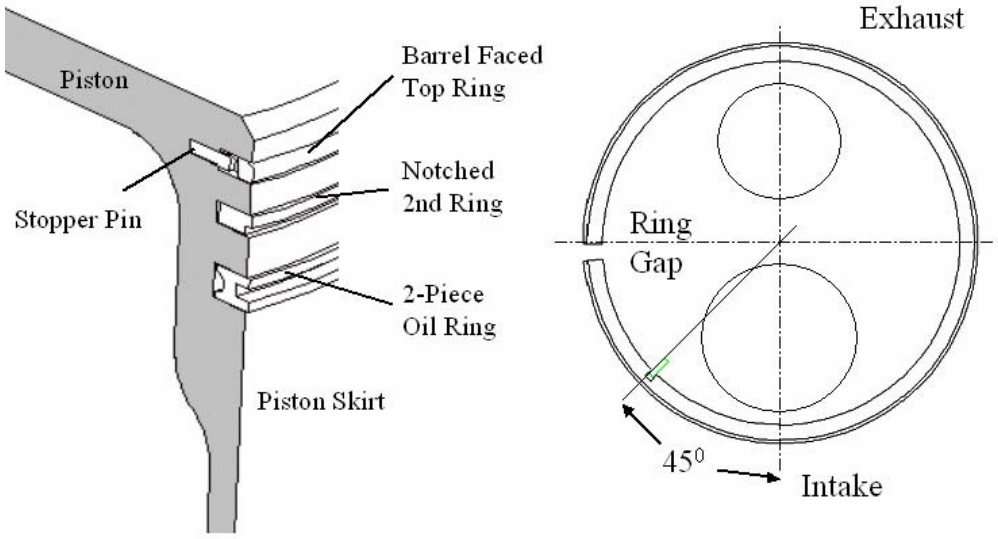

Figure 4-7 Specification of piston ring stopper location

4.4 Sensor Embedding

Electroplating was chosen as the embedding method since it can be deposited in selected areas and has a high strength. It also has the advantage of being a relatively low temperature process so the possibility of damaging the FBG during the embedding process is low as compared to laser deposition of material or embedding by brazing [32,33].

4.4.1 Piston Preparation

Once the piston machining was completed the piston underwent a series of steps to prepare it for the electroplating process. The first step was to clean the residual machining oil by submerging the piston in an ultrasonic acetone bath for five minutes. Afterwards, the piston was dried with compressed nitrogen. To provide a means of holding the piston in the electroplating bath a wire was attached to the inside of the skirt with epoxy. An electrically conductive epoxy (Chemtronics CW2400) was used so that the attached wire could also be

used to connect the piston to the power supply in the electroplating process. To stop the electroplating process from occurring over the entire piston a lacquer mask was applied. Four coats of Tolber Miccrostop lacquer were applied to the entire piston with extra precautions taken to thoroughly coat the ring grooves and wrist pin bosses. After the final application of lacquer the piston was baked at 37 ^{0}C for 20 minutes to ensure that the lacquer had cured.

4.4.2 Chemical Surface Preparation

It is well know that the cleanliness of the substrate, the piston groove in this case, has a direct effect on the quality of the electroplated material. Therefore, a detailed cleaning process was undertaken based on suggested process found in electroplating literature [31,34]. After several iterations the final cleaning process used consisted of the following steps: desmutting, zinc deposition, zinc strip and zinc deposition. To prevent contamination of each chemical bath the piston was washed with a copious amount of deionized water between each step.

A desmut solution removes the residuals left behind in the casting and machining processes. Since the piston used in this research is an A390-T7 alloy it contains significant amounts of silicon as seen in the alloy composition in Table 4.2 to help fluidity in the casting process [31]. These alloying components and residual particles, or smut, have to be removed or problem of porosity or poor adhesion can occur further into the electroplating process. It was found that submerging the piston for one minute in the solution listed in Table 4.3 at room temperature would remove the smut layer.

Component	Al	Cu	Fe	Mg	Mn	Si	Ti	Zn
Weightt %	78	4 - 5	Max 0.5	0.45 - 0.65	Max 0.1	16 - 18	Max 0.2	Max 0.1

Table 4.2 Aluminum A390-T7 casting alloy compostition

	% By Volume
Nitric Acid	20%
Hydrofluric Acid	2%
Dionized Water	Balance

Table 4.3 Desmut and zinc striping solution composition

In addition to surface contaminants, aluminum or magnesium oxidized in varying amounts, or in different forms, can be present. These oxides have to be removed and replaced by a uniform oxide layer otherwise unfavorable electroplating results are likely. By using a zinc deposition process as a pre-electroplating step the oxide layer was chemically removed. The deposited zinc layer protects the aluminum until it is plated. Plating can then occur on a surface clean of oxide since once the part enters the plating solution the zinc is etched away. A layer of zinc was deposited using Caswell Zincate solution used at 20 ^{0}C for 60 seconds. It has been documented in literature [31] that the more uniform the zinc layer is the better the final product will be in terms of bond strength. To obtain a more uniform zinc layer, the first zinc deposit was removed using the solution listed in Table 4.3 and a second layer deposited using the same parameters as the first layer.

4.4.3 Sensor Preparation

By nature optical fibers are not electrically conductive due to the core and cladding being constructed mostly of silica (SiO_2). In addition the buffer layer is generally some type

of polymer material that melts or significantly softens above 100 ^{0}C. Therefore, optical fibers cannot be directly embedded in metal. However, removing the polymer coating and adding a thin metal coating make optic fibers very attractive for use as sensors in metallic structures.

Removing the polymer coating can be accomplished by either a: mechanical stripping or a chemical stripping process. Mechanical stripping is the standard way to remove the polymer coating for telecommunications, however this process tends to leave residual polymer particles stuck to the fiber that have to be removed manually. This can cause the fiber to no longer be chemically clean, and increases the chance of the fiber breaking. When the FBG is written onto the fiber a section of the polymer buffer is stripped away, creating a strength gradient at the end of the stripped section. Using mechanical stripping can cause the fiber to break at this point. Therefore a chemical stripping process was used to remove the polymer coating. When a section of optical fiber containing the FBG was immersed in an acetone bath for ten minutes the polymer buffer layer would detach from the fiber leaving a smooth clean surface.

A thin metallic layer was applied by physical vapor deposition (PVD) to provide an electrically conductive base for embedding. PVD is a method of physically depositing materials including both metals and insulating materials for example Ti or SiO_2. The basic idea of PVD is that an inert gas is ionized and the ions are accelerated into a solid target material. The ions strike the surface of the target material and atomic clusters of the target material are ejected and then deposited onto the sample surface.

The PVD machine used for this research was the CVC 601. The unit has three DC magnetron target stations that can be used, each being able to accommodate various

materials. After argon was injected into the chamber a high vacuum condition was achieved by a cryo-pump. The optical fiber was then sputtered with a 0.05 μm film of titanium and a 0.1 μm film of nickel. The thin titanium film was applied to improve adhesion between the optical fiber and the desired nickel layer. In Table 4.4 the PVD process parameters are described in detail.

Target Material	Titanium	Nickel
Chamber Pressure	0.4 Pa	0.4 Pa
Target Diameter	203.2 mm	76.2 mm
Deposition Power	1 kW	0.5 KW
Ramp Time	10 min	20 min
Film Thickness	50 nm	500 nm

Table 4.4 PVD parameters for titanium and nickel films

4.4.4 Electroplating

Electroplating is the process of depositing a coating having a desirable form by means of electrolysis. A typical electroplating cell consists of anode, cathode, aqueous-metal solution, and a power supply. In the simplified example shown in Figure 4-8, the sacrificial anode is made of nickel, the cathode is made of the material to be electroplated, and the aqueous-metal solution consists of nickel (Ni^{2+}), chlorine (Cl^{1-}) and sulfate ions (SO_4^{2-}). When the power supply is turned on, the positive ions in the solution are attracted to the negatively biased cathode. The nickel ions that reach the cathode gain electrons and are deposited or plated onto the surface of the cathode forming the electrodeposit. Simultaneously, nickel is electrochemically etched from the nickel anode, to produce ions for

the aqueous solution and electrons for the power supply. Hydrogen ions also gain electrons from the cathode and form bubbles of hydrogen gas.

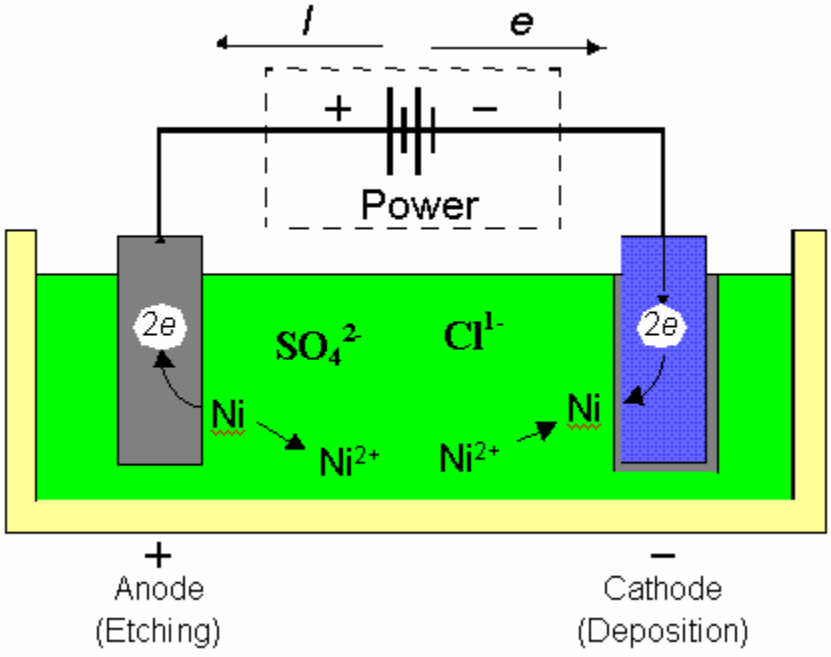

Figure 4-8 Electroplating setup

A copper strike was deposited over the zinc immersion deposit to protect the underlying aluminum. Since the zinc immersion layer is extremely thin, any plating treatment that penetrates the zinc layer will attack the aluminum and a poor deposit will result. Based on literature suggestions [27,34] a copper cyanide solution from Technic Inc. was used with the composition listed in Table 4.5. The strike solution was used at room temperature. Electrical contact was made before immersion of the piston into the bath to limit the deposition that would occur by immersion resulting in the poor adhesion of the

electrodepost. An initial high current density of 26 mA/cm^2 was used for two minutes followed by three minutes at 13 mA/cm^2 to plate approximately 4.5 μm of copper.

Material	Amount (Vol %)
Potassium Copper Cyanide ($K_3Cu(CN)_4$	6.30%
Potassium Cyanide (KCN)	0.65%
Potassium Hydroxide (KOH)	1.00%
Deionized Water	Balance

Table 4.5 Copper strike electroplating bath composition

With the preparation steps completed the FBG sensor was embedded with nickel electroplating. The stainless steel tube was inserted into the locating bosses and the FBG fiber threaded into the tube, at which time the tube and fiber were positioned such that the FBG was in the center of the piston. The temperature of the electroplating bath was controlled to 50 ^{0}C. For the first hour of plating the current density was set to 22.5 mA/cm^2 then adjusted to 40. mA/cm^2 for the duration of the approximate 48 hours of electroplating. The nickel electroplating setup consisted of a polypropylene tub, Micro pump (model HG0024), Gelman Sciences 1 μm filter (CR Capsule model 12829), a Cole-Parmer Digi-Sense Temperature Controller (model 2186-00) with a type J thermocouple, and a quartz laboratory heater (Glo-Quartz model LHP-300).

Material	Amount (Vol %)
Nickel	8.90%
Nickel Sulfate	35.15%
Nickel Chloride	5.86%
Boric Acid	3.90%
Deionized Water	Balance

Table 4.6 Watts nickel electroplating bath composition

4.4.5 Post-Electroplating Preparation

Once sufficient nickel had been deposited to fully embed the sensor, the piston went through several steps to prepare it for engine use including post machining, cleaning and polishing.

Since the localized electrodeposition rate is proportional to the localized current density, a uniform current density over the entire seed layer is needed to obtain an electrodeposit having a uniform thickness. To achieve selective deposition, however, portions of the base material were covered with an insulating masking material that makes the current density in its proximity nonuniform, in addition to the effect from the nonuniform channel geometry. An example of the effect the plating mask has on the uniformity of the current density, and hence the deposition rate, is illustrated in Figure 4-9. This leads to excess deposited nickel on the sides of the channel before the channel center was completely filled. This extra material was removed by milling with a conventional four-flute end mill, as depicted in Figure 4-10. At this time the protective lacquer was removed using acetone in an ultrasonic bath heated to 30 ^{0}C for two ten-minute periods with a water wash in between. Extra nickel was also deposited along the axis of the embedding fiber due to a slight overhang. This was ground away using 400, 600 and 800-grit sandpaper in a Buehler polisher/grinder (model Ecomet II). To polish the ends of the embedded fiber for better light

transmission a solution of colloidal alumina with particle sizes that ranges from 1 μm to 50 nm was used on a 1 μm polishing cloth. The final result is an embedded FBG sensor in an aluminum piston with a mass gain of less than 1 %.

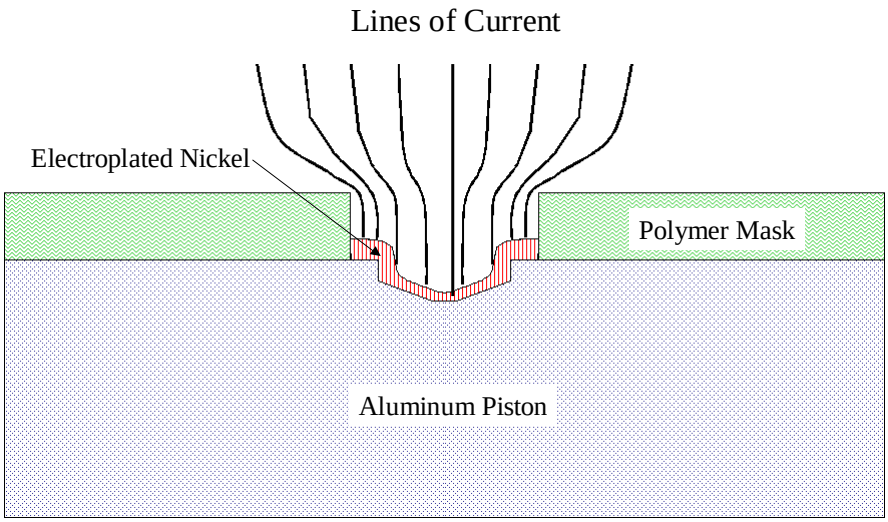

Figure 4-9 Current density variation

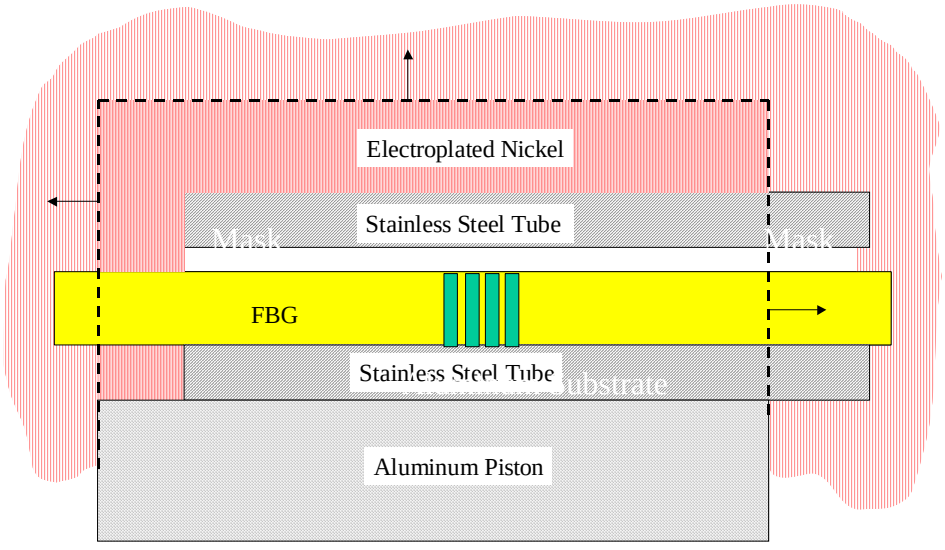

Figure 4-10 Excess deposited nickel

4.4.6 Sensor Placement

Knowing the sensor location is important for future use since the temperature profile can vary greatly over the piston crown area. A piston that had completes the sensor embedding process was sectioned to examine how well the sensor placement differed from the desired location. The piston was cut into four pieces giving a total of eight end views to inspect. A sample cross section in shown in Figure 4-11 as view under 150 times optical magnification. The results of this inquiry were that the vertical placement varied by no more than 0.11 mm from the bottom of the piston channel and less than 0.12 mm deviation from the center of the channel.

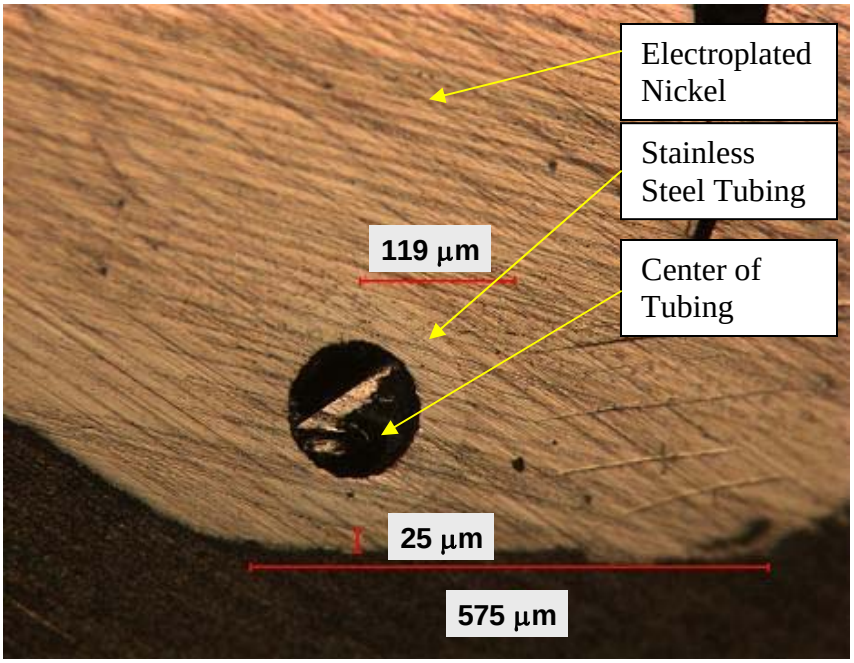

Figure 4-11 Piston section to examine sensor placement

4.4.7 Embedding Issues

The ability to places sensors in places of interest in metallic structures with accuracy and repeatability is important. The main issues are the bonding quality between the nickel layer and the substrate, the positioning of the fiber in the metallic structure and the fragile

end of the optical fibers where they enter and leave the metal part. During manufacturing, two types of defects, delamination and pits, can damage the optical sensors and lower the strength of the embedded sensor or destroy it. However, all types of defects are well documented in literature, along with solutions for each [27,29,31]. Figure 4-12(a) shows a crack at the interface of the base metal and the electroplated material while Figure 4-12(b) shows delimitation of the electroplated material. Surface pits were also present in some samples as seen in Figure 4-12(c). Delamination can be due to inadequate cleaning of the optical fibers and the substrates or improper electroplating parameters such as solution temperature or composition. Pitting is cause by either insufficient agitation or improper cleaning. In addition, unwanted electroplating also occurred on wrist pin and ring groove surfaces as seen in Figure 4-12(d). The cause of this problem was easily identified by close examination of the piston during the lacquer application process and covering any small pores in the lacquer with an additional coating. The embedding quality was improved significantly, as shown in Figure 4-13, after the cleaning process and the electroplating parameters were optimized as described in previous sections. The bonding strength of the electroplated nickel to the substrate was also enhanced by sanding the channel sides before electroplating the part.

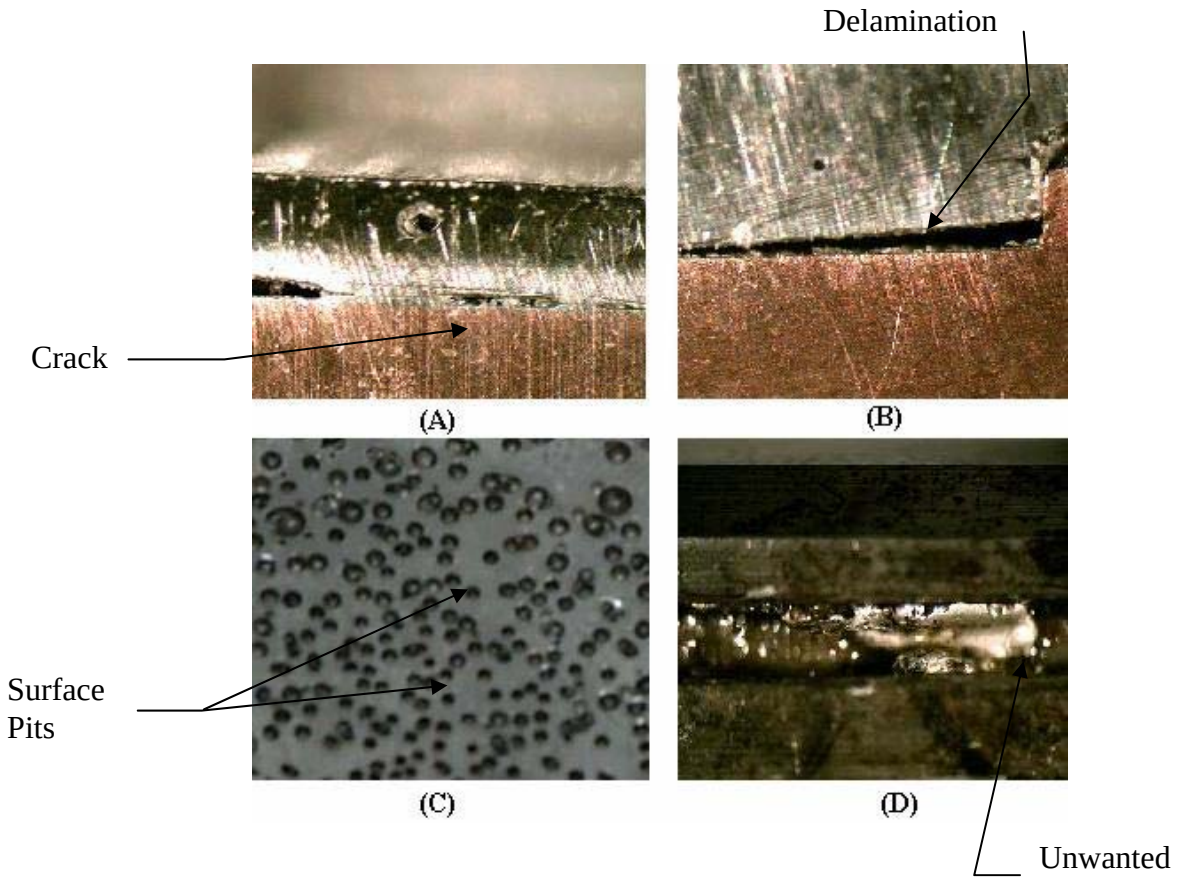

Figure 4-12 Electroplating defects during manufacturing

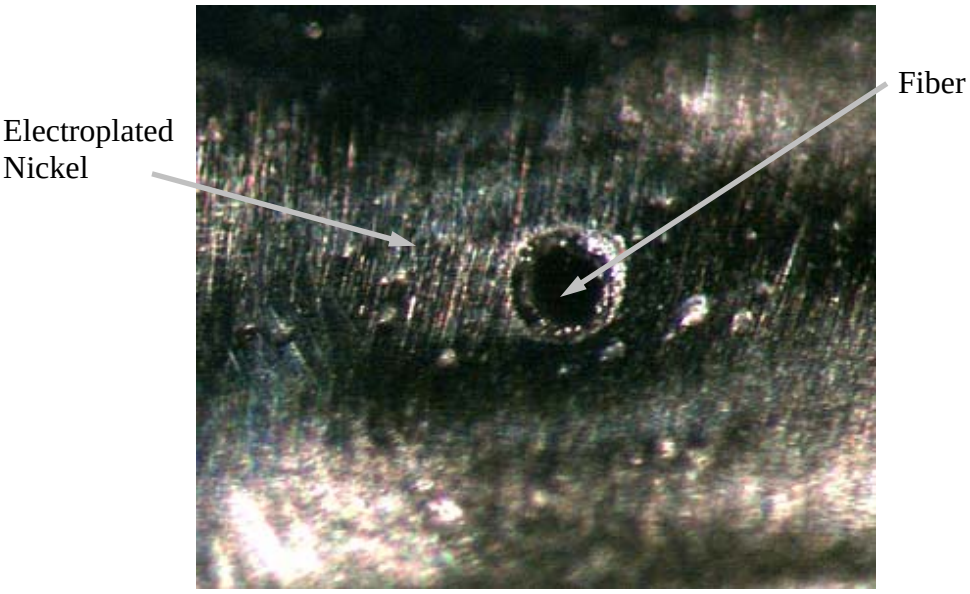

Figure 4-13 Embedded FBG with good bonding, end view showing fiber

4.5 Embedded Sensor Durability

To examine the effects of the embedded sensor on the normal running conditions of the engine a series of tests were performed. A piston containing an embedded fiber was installed into a new cylinder block and motored for a twenty-minute period at 600 RPM. The engine was then disassembled to check the wear incurred. At this point the cylinder was in a like-new state. After reassembling the engine, it was put through another motoring test, this time at the rated speed of 3060 RPM for a thirty-minute period. Inspection of the cylinder and piston revealed no detectable difference. The embedded sensor piston was then put through two firing tests at rated speed and power, each for a thirty-minute duration. In between, the engine was allowed to cool by motoring it at 600 RPM. This time also allowed for an audible inspection of the engine to determine if the operation was abnormal, of which it was not. The engine was disassembled one final time and the cylinder and piston wear were compared to a stock piston run in a new engine for the equivalent time. A comparison of the cylinder bore wear can be seen in Figure 4-14. Noticeable in both pictures is minor cylinder bore scoring, but no deep grooves or wear ridges. The FBG embedding piston was also examined for wear and found to have slight score marks and scuffing of the iron wear coating as can be seen in Figure 4-15. However, despite slight wear both the cylinder and piston were in operable condition.

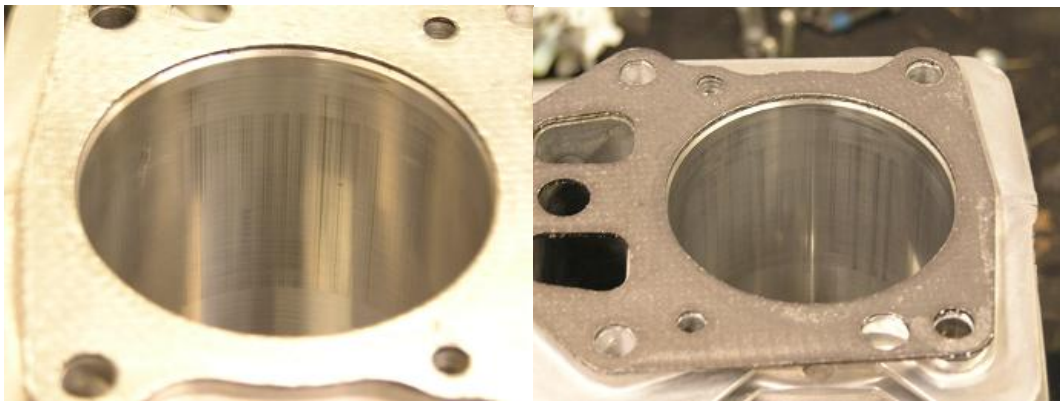

Figure 4-14 Cylinder wear comparison, left: stock engine bore finish and piston right: stock engine bore finish with embedded sensor piston

Figure 4-15 Embedded FBG piston after wear testing

4.6 Embedded Sensor Calibration

The embedded FBG sensor underwent a Bragg Grating wavelength verification and a calibration test to determine its Bragg wavelength shift versus temperature. To establish the curve, the embedded FBG was measured with the broadband source and the OSA. With the piston clamped to an optical table the launching fiber was aligned with the embedded FBG sensor fiber. To accommodate the OSA FC fiber input a 50 μm core fiber was used for light collection with a collimation lens assembly (Thor Labs F230FC-C). This setup led to a total

transmission loss of 83 dB loss from the source to the OSA. The resulting measurement result can be seen in Figure 4-16 along with the supplied grating specifications as received from the manufacturer, O/E Land, in Figure 4-17. In an examination of the two plots it can be seen that the Bragg wavelength matches, but the measured transmission loss was only 3.9 dB at the Bragg wavelength while the stated manufactures loss is 10.5 dB.

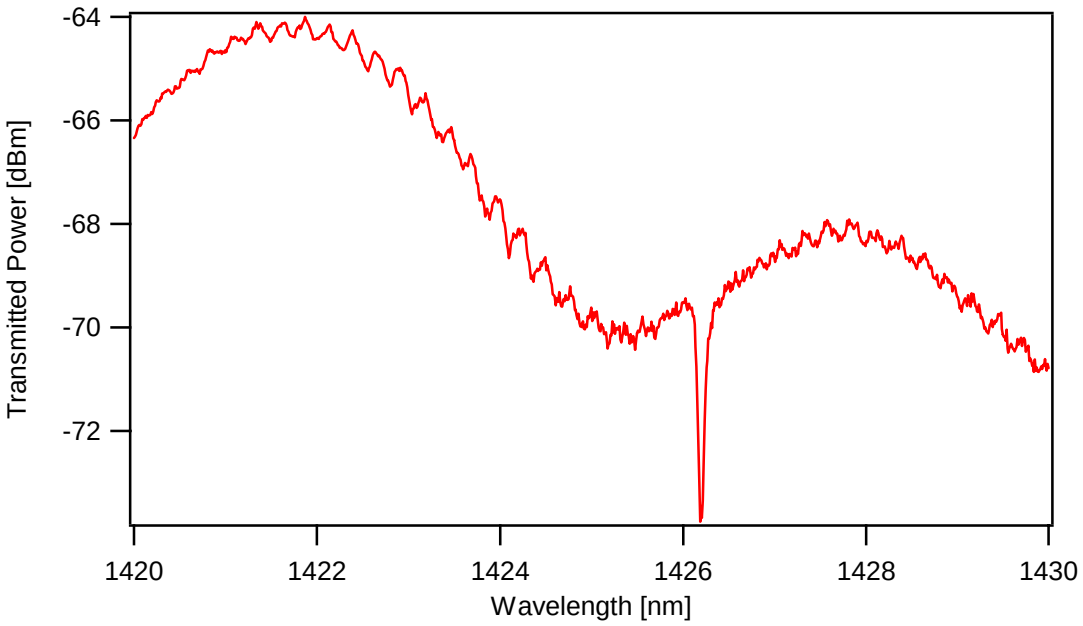

Figure 4-16 Bragg wavelength measurement of embedded sensor with OSA

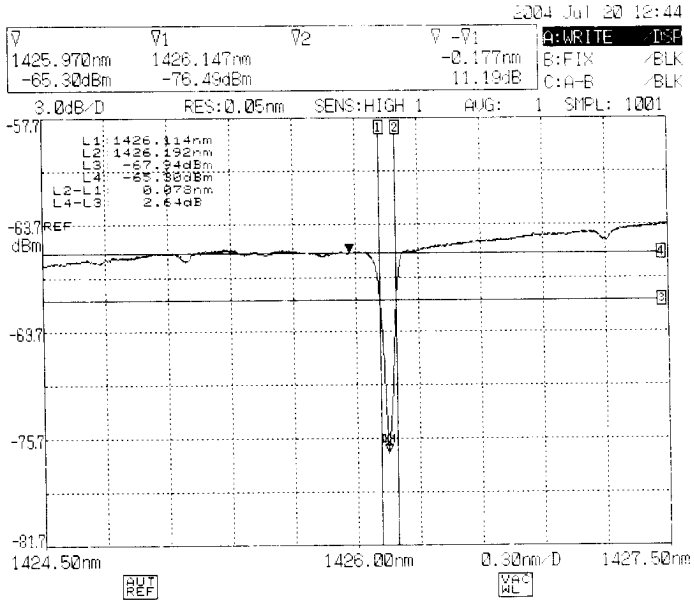

Figure 4-17 Specifications for FBG 14-033-3-8514 as measured by the manufacturer, O/E Land

The sensor calibration test was conducted by placing the entire engine assembly into an oven to raising the entire piston temperature in specified increments. After the oven temperature was changed the engine was allowed to soak for 90 minutes to ensure that the interior piston temperature had reached that of the oven. Temperature readings were then recorded from two K-type thermocouples cemented onto the piston crown and a K-type thermocouple placed inside the oven. A total of eight temperatures were measured extending to 100 ^{0}C.

A typical scan of the slow speed laser is shown in Figure 4-18. This scan shows the Bragg wavelength at 1426.19 nm while at room temperature (20 ^{0}C). It should be noted that at a certain amount of discretization and noise is present in the wavelength output with faster scan speeds. This is due to circuitry than drives the voltage output, when in fact the laser scans at a near constant speed. This could is reduced by slower scan speed but to keep the

recorded data file sizes manageable on the data acquisition computer a moderate scan speed was used.

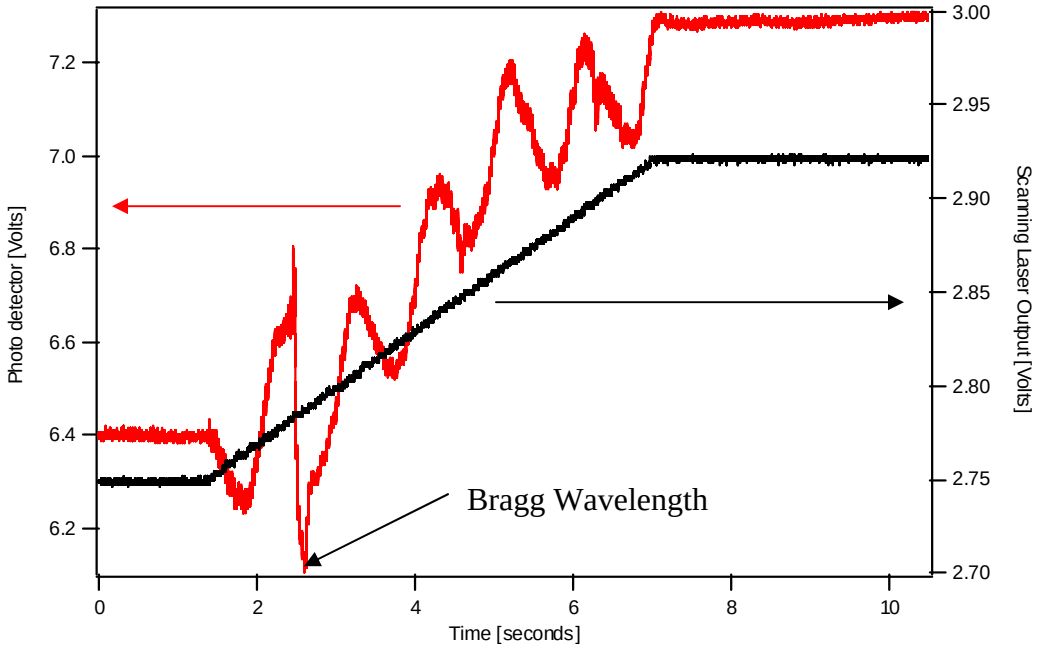

Figure 4-18 Photo detector signal from a laser scan at through the FBG piston at 20 ^{0}C

The composite results of calibration test can be seen in Figure 4-19 with error bars included for the uncertainty of ± 2.2 ^{0}C associated with using K-type thermocouples. As expected, the Bragg wavelength shift with temperature has a linear relationship that can be expressed as:

$$\lambda_B = 0.0112 * T + 1426.1 \qquad (6.2)$$

where T is temperature in degrees Celsius and λ_B is in nm.

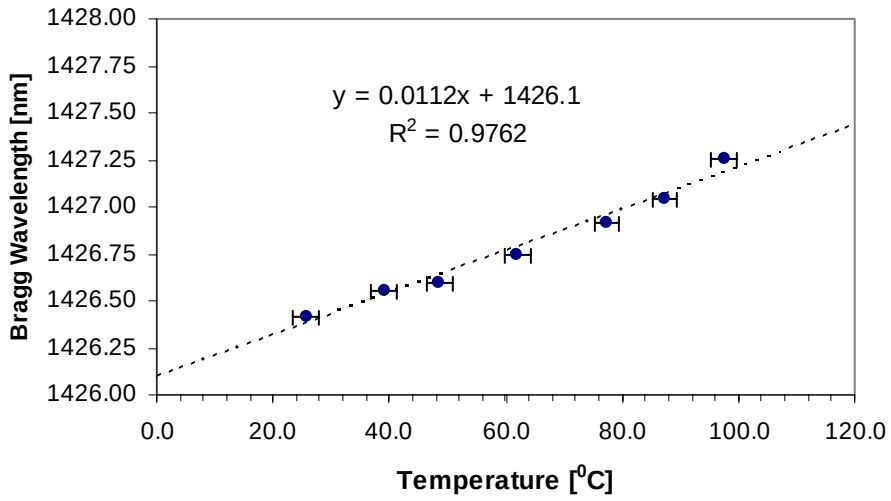

Figure 4-19 Embedded FBG calibration

4.7 Transmission Tribulations

While performing the initial sensor calibration is was noticed that effective transmission was possible in the cladding of the sensor fiber. While using both the broadband source and slow scanning laser it observed that the light signal passing through the FBG did not have the characteristic transmission dip at the Bragg wavelength. However, with slight manipulation of the pitching and collection system the Bragg effect could again be observed. Normally light transmission in the cladding of a fiber optic is quickly stripped away due to the index of refraction mismatches between the cladding and outside environment (normally, air). Since a thin metal film was deposited on the outside of the fiber for electroplating, it is proposed that this film was acting as a mirror keeping the transmission through the cladding at approximated the same efficiency as the core. This would be an important factor later and make alignment in the optical path critical for a high-quality measurement.

5 PISTON TEMPERATURE MEASUREMENT

5.1 Proposed Slow Scanning Solution

A sensing system composed of a slow scanning laser, embedded fiber Bragg grating sensor and the PDA400 photo detector was initially proposed. The tunable diode laser would pitch the light into the FBG and the transmitted light would be collected and measured by the photo detector. Since the FBG reflects one wavelength, the Bragg wavelength, which changes with temperature, the measured transmission time history can be converted to a temperature. Measuring the transmission allows for a larger fiber to be used for collection of light minimizing the coupling loss that would be associated with coupling the light back into the single mode pitching fiber. This method was successful for measuring temperature within a stationary engine. However, the slow scanning laser cannot complete a full wavelength scan during one cycle. Thus, the scan rate would have to be slowed so that the change in wavelength from one, cycle to the next would be small enough to view the FBG transmission loss and be able to get an accurate temperature measurement. If this slow scanning method were implemented it should give results similar to that shown in Figure 5-1. However, using this method proved to be problematic due to fluctuations in the transmitted intensity (i.e. coupling efficiency) measured cycle to cycle. These fluctuations were measured can be seen in Figure 5-2 and vary by an order of magnitude. These variations are more than enough to eclipse the dip in light transmission due to the FBG sensor. To possibly distinguish if this was a collection issue a visible light source was use and the transmitted light observed. With the naked eye variations could easily be seen, qualitatively supporting the measured data variations. Thus, making the temperature measurements with the slow laser scan was not feasible for a running engine with the current optical setup.

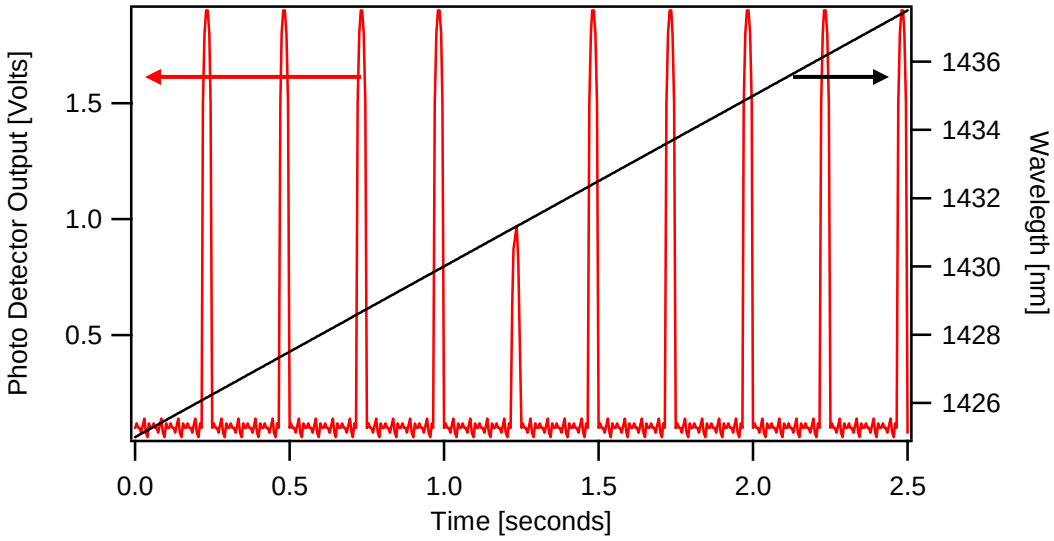

Figure 5-1 Expected results with slow scan laser

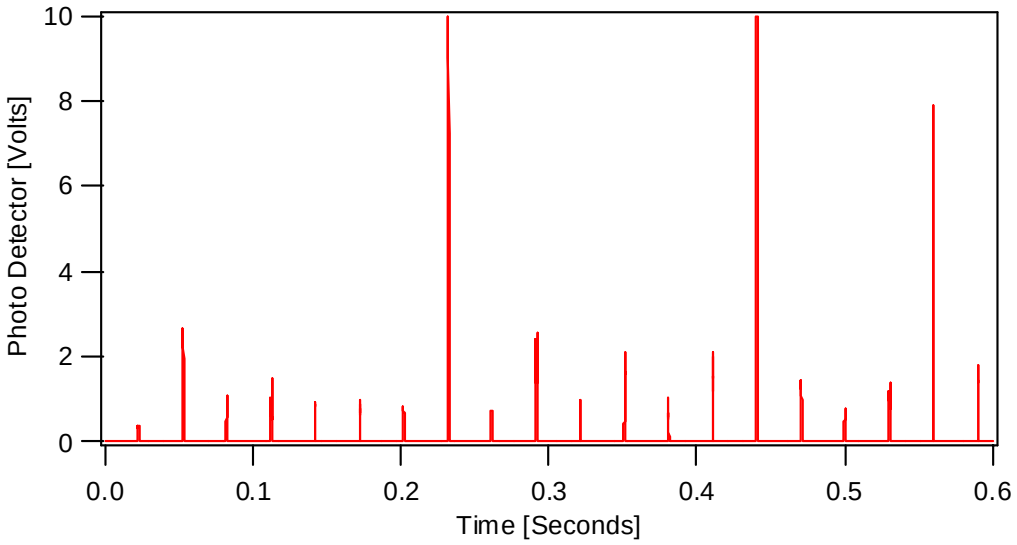

Figure 5-2 Actual fluctuations in transmission from consecutive engine cycles

The slow scanning technique was used to investigate the rise of piston temperature as the engine was warmed up at a full load condition. For this test the engine was controlled to 1700 RPM and full throttle. A 12.5:1 delivered air/fuel ratio corresponded to an IMEP of

719 kPa. To accomplish this measurement a scan was taken at with the engine at rest at room temperature. The engine was then run for three minutes, stopped, the optical path aligned and a temperature measurement taken as soon as possible. At least two more repeat scans were taken to establish a cooling curve for the piston. The piston temperature was linearly extrapolated back to the time when the engine was stopped. The extrapolation process was repeated after running three, six, ten, and twenty minutes for a total engine running time of thirty-nine minutes. The result of the thirty-nine minute running time condition can be seen in Figure 5-3. At the last measurement point the engine oil and exhaust temperatures had stabilized for the previous ten minutes. The results of this process can be seen in Figure 5-4 with the maximum temperature measured to be 149 ^{0}C.

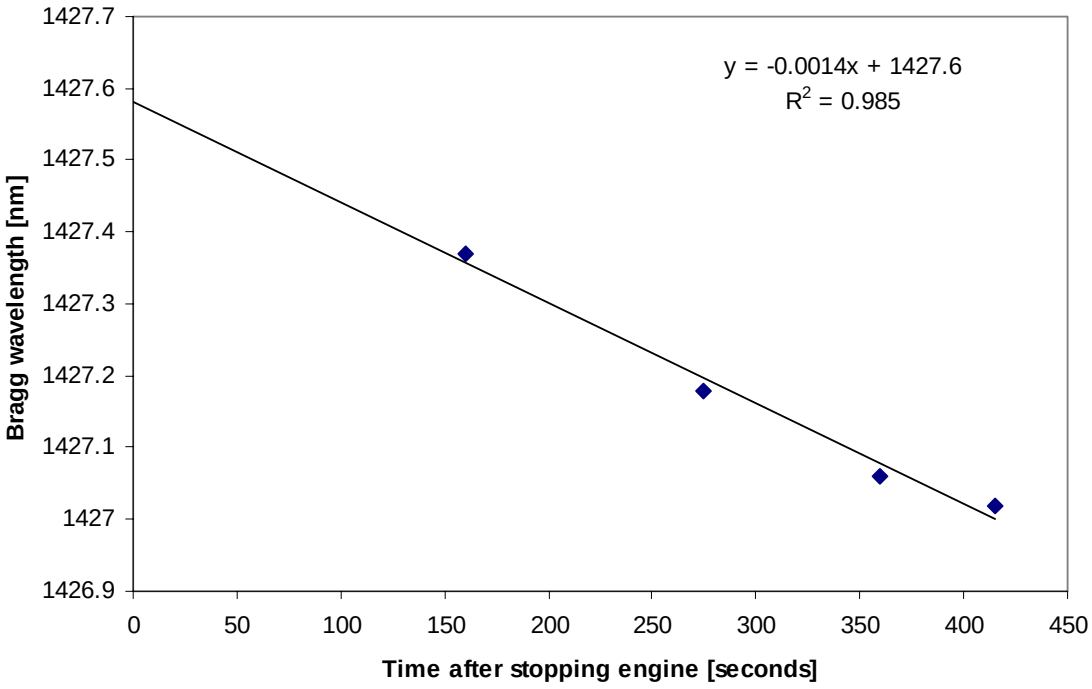

Figure 5-3 Bragg wavelength extrapolation back to engine stop time

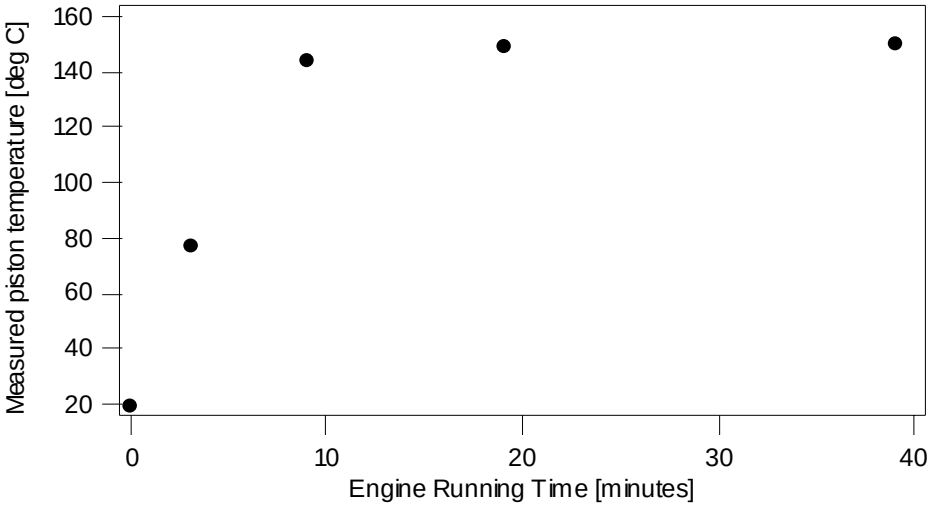

Figure 5-4 Piston temperature variation with running time as measured in a stopped engine

5.2 Proposed Broadband Solution

For the initial confirmation of the embedded FBG a broadband SLED was used as the light source. Therefore, this method was also attempted to measure the Bragg wavelength in a running engine due to the absolute wavelength scale of the OSA and ability to handle future multiple FBG sensors easily. As mentioned previously the OSA is designed to accept single mode fiber with a FC connector. If single mode fiber was used on the collection side, collection side issues were present due to small misalignments in the optical system fabrication. When the large diameter multimode fiber was used and light coupled into a single mode fiber with the correct connections signal loss became an issue. The minimum loss associated with going from the multimode fiber to the single mode was an additional –41 dB due to the etendue principle and thus not allowing enough light transmitted through the single mode fiber for the OSA to record it. These problems were in addition to the problems

faced in the previous section with the slow scanning laser, thus ruling out just this particular combination of FBG and OSA as a means to measure piston temperature in a running engine.

5.3 Fast Scanning Solution

To circumvent the problem of light transmission fluctuations the fast scanning laser was used. From work with the broadband light source and slow scanning laser it was found that the optical path is aligned for the bottom 10 crank angles of each revolution. For the engine operating at the rated speed of 3060 RPM this corresponds to 0.54 ms. Therefore, if the wavelength region of interest can be scanned in less time, cycle to cycle variations in light intensity will not be a factor. Using the fast scanning laser described in a previous section, wavelengths from 1420.20 to 1432.68 nm in 32 μs, well within the time allotted. A MotoTron engine control system was used to supply a trigger at each revolution when the piston had reached BDC. This signal was generated from an unused cylinder spark output since the engine was run on the stock magneto. Using the MotoTron system allowed compensation for small variations in engine speed to occur and still have a triggering point at the same location since the system utilizes a magnetic timing wheel having a resolution of six crank angle degrees. A repeating square wave signal from the rotating mirror was supplied to a circuit, than when it received the MotoTron trigger would then pass the next rotating mirror signal to trigger the data acquisition system. In order to record data fast enough to observe the Bragg wavelength a Tektronix TDS380 oscilloscope was used at 10 MHz to record the voltage signal from the photo detector. To reduce the noise present thirty-two cycles were averaged.

A sample of the raw data measured for the fast scanning laser is presented in Figure 5-5. From this figure it can be seen that the mirror signal lags the laser scan since the

minimum signal output does not correspond to the trigger point. The minimum signal point is located by finding the data point that lies between the two larger dips in signal, which is possible since the wavelength scan is symmetrical. Then the trigger was then shifted using this symmetric relationship until the trigger lined up with minimum data point. The result can be seen in Figure 5-6. Once this was accomplished how the wavelength scan changed with time could be calculated from the known sinusoidal motion of the mirror as shown in Figure 5-7. Due to the fast scan time two measurements were actually taken; one as the laser scans from 1420.20 to 1432.68 nm and another as the laser scans back to 1420.20 nm. A sample trace of this measurement can be seen in Figure 5-8.

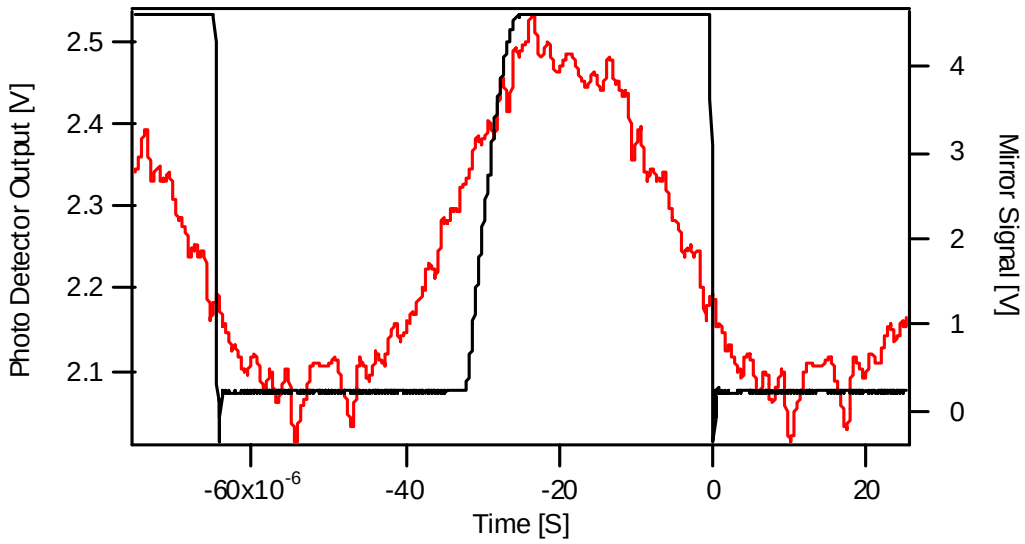

Figure 5-5 Data as collected from the fast scanning laser and mirror output

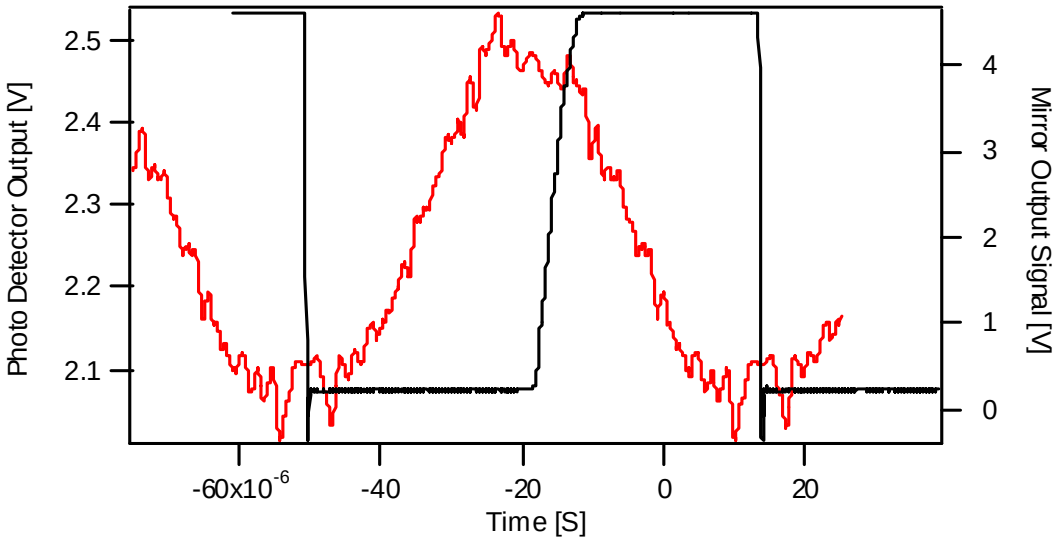

Figure 5-6 Fast scanning laser data with corrected mirror output

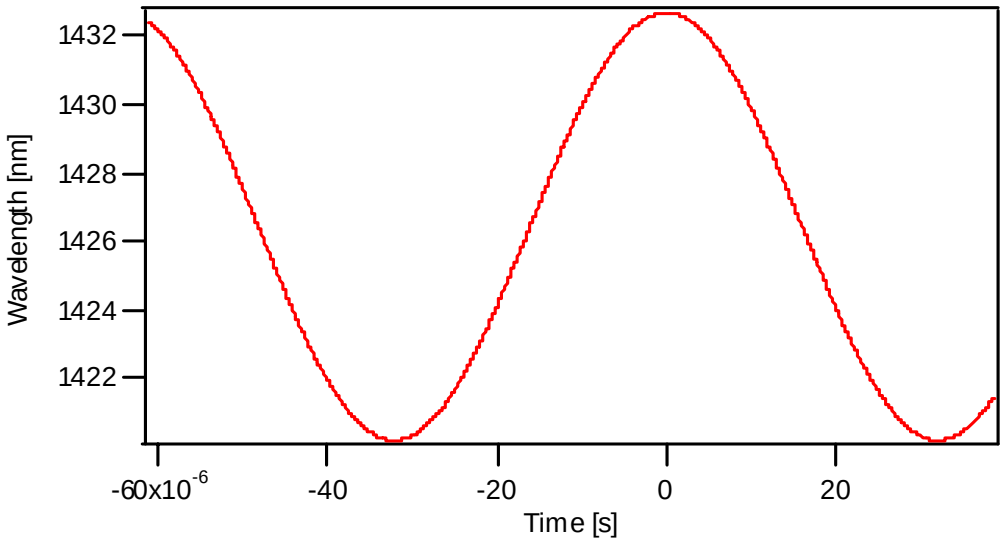

Figure 5-7 Computed wavelength function

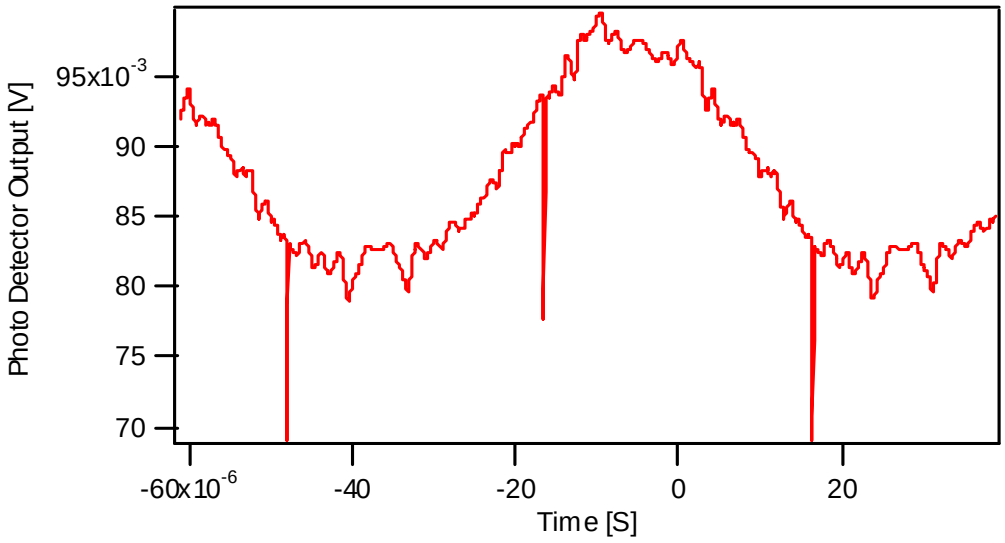

Figure 5-8 Fast laser scan through the FBG sensor while stationary

Three measurements were taking using the fast scanning laser: the engine stationary at room temperature, the engine motoring and the engine firing at the same condition used in the slow scan laser test. A comparison of the three scans can be seen in Figure 5-9. In this comparison only the scan from 1420.20 to 1432.68 nm is shown since the reverse scan generated similar results with a measured wavelength difference of 0.02 nm. The scan taken with the engine stopped at room temperature resulted in a measured temperature of 21.2 ^{0}C with an overall signal loss of 23 dB. The motoring and firing traces had an overall signal loss of 30 dB and resulted in a temperature measurement of 30.1 and 136 ^{0}C, respectfully. Comparing the running temperature measurement with that obtained from the slow scanning laser has the running measurement was 13 ^{0}C lower.

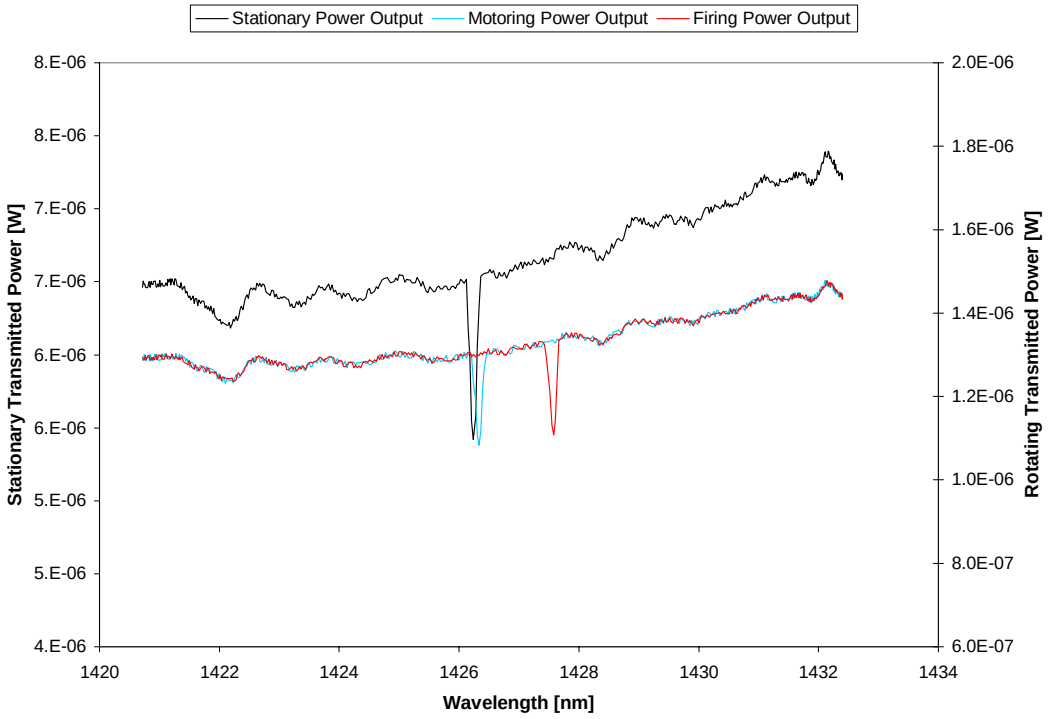

Figure 5-9 Comparison of fast scanning laser through engine with FBG sensor

6 CONCLUSIONS AND RECOMMENDATIONS

6.1 Conclusions

During the course of this project piston temperature was measured in a running internal combustion engine by the use of a FBG sensor embedded into the surface of the piston. To accomplish this goal the engine block was modified for optical access to the cylinder and the piston had a groove machined to allow placement of the sensor. The sensor was embedded into the piston surface using a low temperature electroplating process that leaves the FBG in a functional condition.

Three methods were used to measure piston temperature with a FBG sensor. The slow scan method was plagued by problems of inconsistent light transmission through the engine on a cycle-to-cycle basis. The use of a broadband light source and an OSA was not possible due to the system not being designed as a whole to accommodate this type of measurement. A fast scanning measurement technique was shown to be successful. By completing the wavelength scan fast enough, cycle-to-cycle variations were not an issue. The data measured by the fast scan technique is close to that obtained from measuring the piston temperature of an engine run at similar conditions but stopped. Possible reasons for this could include not identical running conditions or an error in determining the Bragg wavelength while using the fast scanning laser.

6.2 Recommendations

To eliminate most of the problems associated with cycle variation in transmitted light intensity a redesign is recommended for the pitching side optics. While relying on the natural dispersion of light to obtain the desired spot size is the simplest, it by no means provides the flexibility needed to compensate for the motion in an internal combustion

engine. In addition the use of a more precise fiber adjustment stage would be helpful. The manufacturing tolerances, while small prove to be detrimental in aligning the pitching side, often requiring a long tedious process of trying to located the sensor by gross adjustments of the X and Y stages. If some sort of adjustment was also allowed for on the collection side, it may be possible to use a smaller fiber and thus be able to use the OSA for capturing the transmitted signal.

The specifications of the FBG to be embedded into a piston should be checked before the embedding process is undertaken. As seen in this research, the Bragg wavelength reflection was not as strong as claimed by the manufacture. A prescreening operation would rule out the use of a damaged sensor before undertaking the precise process of embedding the FBG.

The project as reported in this thesis involved only taking piston temperature measurement at only one operating condition. In order to further study engine heat transfer a further investigation should be undertaken to examine the effects of various operating parameters. As suggested in other literature the effects of engine speed, load and fuel mixture are thought to be major influences in piston temperature and should be investigated. While only limited knowledge can be gained by using the current single point temperature measurement it may prove insightful to overall engine heat transfer.

Certainly the addition of more FBG would be useful to understand heat flows within the piston. An embedded FBG array would give a more precise account of how temperature varies spatially within the piston by adding multiple sensing locations. Having this additional data would allow simulation boundaries to be examined, leading to more accurate models. While an array of thermocouples would add to the complexity of the data

processing, the fast scanning laser has the additional wavelengths available to accommodate several additional sensors.

In this project the FBG sensor was embedding using a foreign material not normally used in a piston thus effecting heat flow through the piston. If the FBG embedding process could be integrating into the original manufacturing process the FBG technique would provide a more realistic picture of the temperature distribution in an uninstrumented piston. This would also allow for the most flexibility in placing the FBG sensors in locations that would be of most interest.

7 REFERENCES

1. Kalpakjian and Schmid, Manufacturing Engineering and Technology, Prentice Hall, 2001.

2. Heisler, Heinz, Vehicle and Engine Technology, Society of Automotive Engineers, 1999.

3. Heywood, J., Internal Combustion Engine Fundamentals, New York, McGraw-Hill Inc., 1988.

4. Gibson, A., "Piston Temperature and Heat Flow in High Speed Petrol Engines". Proceedings of the Institute of Mechanical Engineers 1926.

5. Baker, H. "The Operating Temperatures of Cast Iron and Aluminum Pistons in a 12 Inch Bore Oil Engine". Proceedings of the Institute of Mechanical Engineers 1937.

6. Hepworth, J., "Piston Assemblies for Road Transport Oil Engines". Institute of Mechanical Engineers Automobile Divisional Proceedings 1950.

7. Pinski, F., "Temperature Measurement of Internal Combustion Engine Pistons". Measurement Techniques. Number 7 1964.

8. Underwood, A., Catlin, A., "An Instrument for Continuous Measurement of Piston Temperatures". SAE Transactions, Volume 48, Number 1, 1941.

9. Walker, J., "Piston Temperature Measurements in a Watercooled Two Stroke Cycle Spark Ignition Engine M.S. Thesis, Mechanical Engineering Department, University of Wisconsin-Madison, 1966.

10. Barna, G., Brumm, D., Anderson, C., "An infrared telemetry technique for making piston temperature measurements" SAE Technical Paper 910051, 1991.

11. Burrahm, R., Davis, J., Perry, W., De Los Santos, A., "Development of a piston temperature telemetry system" SAE Technical Paper 920232 1992.

12. Kato, N., Matsui, M., Shimura, T., Moritsugu J., "Piston Temperature Measuring Technology Using Electromagnetic Induction, "SAE Technical Paper 2001-01-2027, 2001.

13. Templug User Information Guide, Revision 3.0 April 2004.

14. R. Measures, R. Maaskant, T. Alaview, G. Tadros, S. Rizkalla, A. Thakurta, "Fiber-optic Bragg gratings for bridge monitoring," *Cement and Concrete Composites*, **9**, pp21-23, 1997.

15. X. Li, F. Prinz, Embedding of Fiber Optic Sensors in Layered Manufacturing, *Proc. Eleventh Solid Freeform Fabrication Symposium*, 2000.

16. T. Bosselmann, Magneto- and electro-optic transformers meet expectations of power industry, *Proc. OFS'12*, pp111-114, 1997

17. K. Nagashima, K. Tsunemichi, K. Tsuchiya, Indicated Mean Effective Pressure Measuring Method Using Optical Fiber Pressure Sensor 2003-01-2013, 2003

18. Udd, U., ed., Fibre-Optic Smart Structures, Wiley, New York, 1995.

19. X. Li, F. Prinz, Non-contact Strain and Temperature Measurement for Rotating Parts with Embedded Fiber Optic Sensors, Measurement Science and Technology, 2002.

20. Hill, K., Fuji, Y., Johnson, D., Kawaski, B., "Photosensitivity in Optical Fiber Waveguides: Application to Reflection Filter Fabrication". Applied Physics Letters Vol. 32, 1978, pp. 647-649.

21. Kawaski, B., Hill, K., Johnson, D., Fuji, Y., "Narrow-band Bragg Reflections in Optical Fibers". Optics Letters, Vol. 3, 1978, pp. 66-68.

22. Othonos, A., Kalli, K., Fiber Bragg Bratings: Fundamentals and Applications in Telecommunications and Sensing, Boston, Artech House optoelectronics library, 1999

23. Albert, B., "Residual Gas Effects On Combustion In An Air-Cooled Utility Engine", M.S. Thesis, Mechanical Engineering Department, University of Wisconsin-Madison, 2004.

24. Kranendonk, L.A., Walewski, J.W., Tongwoo, K., Sanders, S.T., "Wavelength-agile sensor applied for HCCI engine measurements. " 30th International Symposium on Combustion, Chicago, IL., 2004.

25. Saito, K., Kohama, T., Basaki, M., Suzuki, T. "The visualization analysis of the behavior of piston ring" JSAE Technical Paper No. 9941647, 1999.

26. Schneider, E., Blossfeld, D., "Method for Measurement of Piston Ring Rotation in an Operating Engine", SAE Technical Paper 900224, 1990.

27. Brugger, R., Nickel Plating, Teddington, Robert Draper LTD, 1970

28. Durney, L., Electroplating Engineering Handbook, New York, Van Nostrand Reinhold Company, 1984.

29. Handbook on Electroplating, Birmingham, W Canning & Co. LTD, 1966

30. Iida, Y., Tanaka, K., Fuse, S., "Contact-Point Method for Measuring Sliding Face Temperature and Its Applications", SAE Technical Paper 830311, 1983.

31. King, R.G., Surface Treatment And Finishing Of Aluminum, Oxford, Pergamon Press 1988.

32. Li, X., "Embedded Sensors in Layered Manufacturing", PhD Thesis, Mechanical Engineering Department, Stanford University, 2001.

33. Sandlin, A., Jeskanen, H., Li, X., Björklöf, A., "Manufacturing and Quality Evaluation of Component Integrated Fibre Optical Sensors For Condition Monitoring",

34. Lowenheim, F.A., Modern Electroplating, New York, John Wiley & Sons, Inc 1963.

35. Mierbach, A., Duck, G., Newman, B., "Heat Flow Through Piston Rings and Its Influence on Shape", SAE Technical Paper 831283, 1983.

APPENDIX A – PRESSURE TRANSDUCER CALIBRATION